

Projecting Global Mercury Emissions and Deposition Under the Shared Socioeconomic Pathways

Benjamin M. Geyman¹, David G Streets¹, Colin P Thackray¹, Christine Olson², Kevin M. Schaefer², and Elsie M. Sunderland¹

¹Harvard University

²University of Colorado Boulder

November 8, 2023

Abstract

Mercury (Hg) is a naturally occurring element that has been greatly enriched in the environment by activities like mining and fossil fuel combustion. Despite commonalities in some CO₂ and Hg emission sources, the implications of long-range climate scenarios for anthropogenic Hg emissions have yet to be explored. Here, we present comprehensive projections of anthropogenic Hg emissions (2020-2300) and evaluate impacts on global atmospheric Hg deposition. Projections are based on four shared socioeconomic pathway (SSP) narratives ranging from sustainable reductions in resource and energy intensity to rapid economic growth driven by abundant fossil fuel exploitation. There is a greater than two-fold difference in cumulative anthropogenic Hg emissions between the lower-bound (110 Gg) and upper-bound (230 Gg) scenarios. Hg releases to land and water are approximately six times those of direct emissions to air (600-1470 Gg). At their peak, anthropogenic Hg emissions reach 2200-2600 Mg a⁻¹ sometime between 2010 (baseline) and 2030, depending on the SSP scenario. Coal combustion is the largest determinant of differences in Hg emissions among scenarios. Decoupling of Hg and CO₂ emissions sources occurs under low- to mid-range scenarios, though contributions from artisanal and small-scale gold mining remain uncertain. A projected future shift in speciation of Hg emissions toward lower gaseous elemental Hg (Hg₀) and higher divalent Hg (Hg_{II}) will result in a higher fraction of locally-sourced Hg deposition. Projected re-emissions of previously deposited anthropogenic Hg follow a similar temporal trajectory to primary emissions, amplifying benefits of primary Hg emissions reductions under the most stringent mitigation scenarios.

1

2 **Projecting Global Mercury Emissions and Deposition Under the Shared** 3 **Socioeconomic Pathways**

4 Benjamin M. Geyman¹, David G. Streets¹, Colin P. Thackray,¹ Christine L. Olson², Kevin
5 Schaefer², and Elsie M. Sunderland^{1,3}

6 ¹Harvard John A. Paulson School of Engineering and Applied Sciences, Cambridge, MA 01238, USA.

7 ²National Snow and Ice Data Center, Cooperative Institute for Research in Environmental Sciences, University of
8 Colorado Boulder, Boulder, CO, USA.

9 ³Department of Environmental Health, Harvard School of Public Health, Boston, Massachusetts 02115, USA.

10 Corresponding author: Benjamin Geyman (bgeyman@fas.harvard.edu)

11 **Key Points:**

- 12 • Future (2010-2300) anthropogenic Hg releases to air, land and water (0.7-1.7 Tg) are
13 similar to historical (1510-2010) releases (1.1-2.8 Tg)
- 14 • Cumulative anthropogenic Hg emissions to air (2010-2300) vary by a factor of two
15 across scenarios (110-230 Gg)
- 16 • Deposition declines from near-term reductions in anthropogenic Hg emissions are
17 amplified by reductions in re-emissions from land and ocean

18 **Abstract**

19 Mercury (Hg) is a naturally occurring element that has been greatly enriched in the environment
20 by activities like mining and fossil fuel combustion. Despite commonalities in some CO₂ and Hg
21 emission sources, the implications of long-range climate scenarios for anthropogenic Hg
22 emissions have yet to be explored. Here, we present comprehensive projections of anthropogenic
23 Hg emissions (2020-2300) and evaluate impacts on global atmospheric Hg deposition.
24 Projections are based on four shared socioeconomic pathway (SSP) narratives ranging from
25 sustainable reductions in resource and energy intensity to rapid economic growth driven by
26 abundant fossil fuel exploitation. There is a greater than two-fold difference in cumulative
27 anthropogenic Hg emissions between the lower-bound (110 Gg) and upper-bound (230 Gg)
28 scenarios. Hg releases to land and water are approximately six times those of direct emissions to
29 air (600-1470 Gg). At their peak, anthropogenic Hg emissions reach 2200-2600 Mg a⁻¹ sometime
30 between 2010 (baseline) and 2030, depending on the SSP scenario. Coal combustion is the
31 largest determinant of differences in Hg emissions among scenarios. Decoupling of Hg and CO₂
32 emissions sources occurs under low- to mid-range scenarios, though contributions from artisanal
33 and small-scale gold mining remain uncertain. A projected future shift in speciation of Hg
34 emissions toward lower gaseous elemental Hg (Hg⁰) and higher divalent Hg (Hg^{II}) will result in
35 a higher fraction of locally-sourced Hg deposition. Projected re-emissions of previously
36 deposited anthropogenic Hg follow a similar temporal trajectory to primary emissions,
37 amplifying benefits of primary Hg emissions reductions under the most stringent mitigation
38 scenarios.

39 Plain Language Summary

40 Mercury is a global pollutant that is emitted alongside greenhouse gases like carbon dioxide
41 (CO₂) when fossil fuels such as coal are burned. Researchers have projected how emissions of
42 greenhouse gases and climate are likely to change in the future, but relatively little is known
43 about future Hg releases. Here, we project future Hg emissions between 2020 and 2300 using
44 growth scenarios developed by climate change researchers. Under low emission scenarios, Hg
45 emissions are projected to peak between 2010 and 2030. Under the high emission scenario, Hg
46 releases continue near present-day levels until after 2060, and decline more slowly than other
47 scenarios thereafter. Large variability in projected releases (cumulatively a two-fold difference)
48 is apparent across the low and high scenarios. Globally, the intensity of coal combustion and
49 how quickly it is phased out is the largest driver of future Hg releases. We then use global
50 models to simulate future atmospheric Hg deposition, identifying multiple factors responsible for
51 changing deposition patterns and amounts. We find there is a penalty for delaying reductions in
52 Hg emissions because of increased reemissions from the land and ocean in the future. This work
53 emphasizes the benefits of near-term stringent global reductions in anthropogenic Hg releases.

54 1 Introduction

55 Mercury (Hg) is a naturally occurring element, but human activities such as mining and fossil-
56 fuel combustion have released approximately 1.5 Tg of Hg from stable geologic reservoirs to the
57 atmosphere, land, and water over the past 500 years (1510–2010) (Streets et al., 2019a). This has
58 significantly altered the natural biogeochemical Hg cycle (Geyman et al., 2023; Streets et al.,
59 2019a) and adversely affected the health of exposed humans and wildlife (Basu et al., 2023).
60 Reemission of anthropogenic Hg from terrestrial and aquatic ecosystems extends its lifetime in
61 the biosphere (referred to as “legacy Hg”). Past work has quantified the impacts of historical
62 emissions and legacy Hg cycling on the global Hg cycle (Amos et al., 2013; Angot et al., 2018;
63 Guerrero & Schneider, 2023; Nriagu, 1994). However, estimates of future anthropogenic Hg
64 emissions based on the most recent future growth scenarios adopted by the Intergovernmental
65 Panel on Climate Change (IPCC) and their drivers are not presently available (O’Neill et al.,
66 2016), limiting our ability to project future scenarios of Hg pollution.

67 Shared Socioeconomic Pathways (SSPs) and associated emission scenarios offer unified
68 narratives ranging from sustainable development to fossil fuel-driven growth (O’Neill et al.,
69 2016, 2017). They provide a framework for bounding development and greenhouse gas
70 trajectories extending to the year 2300 (Meinshausen et al., 2020). However, these narratives do
71 not explicitly address Hg emissions or the technological transformations underpinning future
72 changes in Hg emission intensity. We fill this gap by developing a methodology for projecting
73 time-dependent change in activity-specific Hg emission factors. This approach is built upon
74 detailed parameterizations developed for historical emission inventories (Streets et al., 2011,
75 2019a), which facilitates intercomparison of past and future emissions.

76 Anthropogenic Hg is released to the atmosphere in both the elemental (Hg⁰) and oxidized (Hg^{II})
77 forms. Hg^{II} has an atmospheric lifetime against deposition of a few days (Corbitt et al., 2011),
78 while the lifetime of Hg⁰ is greater than one year (Horowitz et al., 2017; Shah et al., 2021).
79 Previous studies projected Hg deposition in 2035 and 2050 based on anthropogenic Hg
80 emissions estimated from older IPCC Special Report on Emission Scenarios (SRES) and

81 independent estimates (Corbitt et al., 2011; Pacyna et al., 2016; Streets et al., 2009). Results
82 suggested future increases in Hg^{II} emissions relative to Hg^0 are likely to increase the proportion
83 of regional Hg deposition from emitting countries. The SRES emission trajectories ranged from a
84 best-case scenario that showed relatively flat anthropogenic Hg emissions between 2006 and
85 2050, to a scenario characterized by higher energy and economic growth (A1B) that
86 approximately doubled 2006 emissions levels (Streets et al., 2009). Results from Pacyna et al.
87 (2016) ranged from a slight increase under a current policy scenario to -85% under a maximum
88 feasible reduction case. However, these past studies did not consider future changes in marine
89 and terrestrial Hg reservoirs that affect reemission of Hg^0 (Amos et al., 2013, 2014). This is
90 important because terrestrial and marine Hg^0 evasion are thought to account for large fractions of
91 the atmospheric Hg undergoing contemporary and future deposition (e.g., ~60% of 2050
92 deposition to the contiguous United States) (Corbitt et al., 2011).

93 The main objective of this work was to better understand how future anthropogenic Hg
94 emissions and deposition vary among the most recent socioeconomic development pathways
95 used by the IPCC. To do this, we developed new decadal projections of primary anthropogenic
96 Hg emissions for the years 2020-2300 based on four distinct SSPs spanning a wide range of
97 radiative forcings. Using a suite of global modeling tools, we quantified how changes in primary
98 Hg emissions and re-emissions from terrestrial and marine ecosystems affect regional
99 magnitudes and global patterns in atmospheric deposition. This work provides insights into how
100 different fossil fuel use scenarios are likely to affect global Hg burdens and the potential effects
101 of different pollution control efforts.

102 **2 Methods**

103 2.1 Description of Development Narratives (SSP Scenarios)

104 Forecasts of future anthropogenic Hg emissions were developed in accordance with the scenarios
105 used in Phase 6 of the Coupled Model Intercomparison Project (CMIP6), organized under the
106 auspices of the IPCC (O'Neill et al., 2016). The scenarios were based on a framework combining
107 narratives of global development with emissions and climate projections from integrated
108 assessment and climate models (O'Neill et al., 2016). The first component, the SSPs, are
109 comprised of five distinct narratives describing alternative courses of societal development, as
110 well as quantitative descriptions of population, economic growth, and urbanization (Dellink et
111 al., 2017; Jiang & O'Neill, 2017; Kc & Lutz, 2017). The SSPs were elaborated using integrated
112 assessment models (IAMs) to provide quantitative descriptions of energy use, greenhouse gas
113 emissions, and land-use change (Riahi et al., 2017).

114 For each SSP narrative, multiple IAM trajectories were defined to describe both a baseline
115 scenario, which assumes no additional climate policies or climate change impacts, and mitigation
116 scenarios, in which further policies are adopted. SSP narratives can be combined with different
117 climate forcing pathways to describe the physical response of the climate system. The climate
118 forcing is defined according to the long-term global average radiative forcing (W m^{-2} ; Myhre et
119 al., 2013). Following convention, the scenarios used in this work are written as: SSP_{x-y} , where x
120 is the SSP and y is the radiative forcing pathway (W m^{-2}) (O'Neill et al., 2016). Throughout the
121 rest of this work, scenarios will be referred by their specific name (e.g., SSP1-2.6) or collectively
122 as “SSPs.”

123 For this work, we adopted the three major scenarios that were initially chosen for long-term
 124 extensions (LTE) to 2300 under CMIP6 (O'Neill et al., 2016), namely, SSPs 1-2.6, 5-3.4, and 5-
 125 8.5. Scenario SSP1-2.6 is a lower-bound on future emissions, reflecting strong emphasis on
 126 sustainability and intensive control of climate-forcing agents; SSP5-3.4 is known as the
 127 “overshoot” scenario and reflects short-term growth in fossil-fuel use and minimal consideration
 128 of climate control measures until 2040 followed by aggressive mitigation thereafter; SSP5-8.5 is
 129 an upper bound on emissions, in which fossil-fuel use continues with little consideration of
 130 climate mitigation or transition to clean technologies. Subsequently, Meinshausen et al. (2020)
 131 extended additional scenarios to beyond 2300, so we added a fourth scenario to our projections,
 132 the so-called “middle-of-the-road” scenario, SSP2-4.5 (Fricko et al., 2017).

133 The detailed raw activity data that are used in this work to characterize Hg emissions under these
 134 four scenarios out to 2100 follow the work of Rao et al. (2017), with LTE from 2100 to 2300
 135 following the work of Meinshausen et al. (2020). The Hg emissions forecasts reported in this
 136 work map the trajectories of CO₂ forecasts contained in the previously mentioned publications
 137 and the emissions of other species as described in subsequent studies (Gidden et al., 2019; Lund
 138 et al., 2019; Turnock et al., 2020). However, this work contains the first reported projections of
 139 Hg emissions under CMIP6 scenarios.

140 The SSP scenarios were used primarily to project fossil-fuel use (coal and oil), the manufacture
 141 and use of refined industrial products, and economic parameters. However, there are no specific
 142 variables from which to calculate the extraction and production of raw materials and basic
 143 products because these are not directly relevant to emissions of greenhouse gases. However, they
 144 are very important as sources of mercury. Thus, for 21st century production of these materials,
 145 we used forecasts specifically generated by industry models, as follows: copper, zinc, and lead
 146 (Sverdrup et al., 2019); iron (Morfeldt et al., 2015); mercury (Sverdrup & Olafsdottir, 2020); and
 147 gold (Sverdrup et al., 2012); as well as the basic industrial products steel (Morfeldt et al., 2015)
 148 and cement (Zhang et al., 2018). The work of Watari et al. (2020, 2021) was valuable in guiding
 149 the pathways of metals extraction and use to the end of the century.

150 2.2 Mercury Emission Calculation

151 Mercury emissions under a future climate scenario (f) were calculated using Equation (1):

$$E_{t,r,s,f} = E_{2010,r,s} \times \left(\frac{A_{t,r,s,f}}{A_{2010,r,s,f}} \right) \times \left(\frac{EF_{t,r,s,f}}{EF_{2010,r,s,f}} \right), \#(1)$$

152 where E = emissions (Mg a⁻¹); t = decadal future year, r = world region, s = source type; A =
 153 activity level (in various units); and EF = emission factor (g per unit of activity).

154 Future Hg emissions were calculated by extrapolating 2010 base-year emissions, as reported in
 155 (Streets et al., 2017, 2019a), in accordance with the energy and activity forecasts for each of the
 156 four future scenarios (f) described in the previous section. Emissions were calculated for each
 157 decade between 2020 and 2300, though they reach zero between 2190 and 2250 across scenarios
 158 in accordance with SSP prescriptions. Emissions are zero beyond 2250 across all scenarios.

159 Emissions were calculated at world region level (r). The SSP forecasts were developed for five
 160 world regions: OECD, REF (Russia and Eastern Europe), ASIA, MAF (Middle East and Africa),
 161 and LAM (Latin America). This is a very coarse division of the world, which may be adequate
 162 for CO₂ studies, but is too aggregated for studies of Hg emissions and transport. In particular, the
 163 OECD region is spread across the globe, with contributions from Western Europe, North
 164 America, Australasia, and Japan. The prior Hg emission estimates for 2010 (Streets et al., 2019a,
 165 2019b), upon which this work is based, were calculated for 17 world regions and subsequently
 166 aggregated to seven: North America (NAM), South America (SAM), Western Europe (EUR), the
 167 Former Soviet Union (FSU), Africa/Middle East (AFM), Asia (ASA), and Oceania (OCA). By
 168 examining 2010 Hg emissions in the world regions used in each of these two studies, a simple
 169 equivalence was determined and applied in this work, as follows: NAM = 0.5 OECD + 0.1
 170 LAM; SAM = 0.9 LAM; EUR = 0.3 OECD; FSU = REF; AFM = MAF; ASA = ASIA + 0.05
 171 OECD; and OCA = 0.15 OECD. Emissions at the global scale (GLO) are thus identical. Though
 172 this is less than an ideal solution—because of potential future differences in the rates of
 173 development among the countries comprising the coarse SSP regions—it is certainly an
 174 improvement over the five SSP regions from the perspective of estimating Hg transport and
 175 deposition.

176 The SSP scenarios contain more than 600 activity components (A), covering all aspects of future
 177 energy, industrial, and economic development. The prior 2010 Hg emission estimates were
 178 developed for 18 source types (s) (Streets et al., 2017). Because none of the SSP scenarios
 179 provide activity components that can be unequivocally associated with several of the Hg source
 180 types, emissions from 11 source types were projected individually in this work: mining (copper,
 181 zinc, lead, iron, mercury, gold, and artisanal gold), steel production, cement production, coal
 182 combustion, and oil combustion. Six other source types (municipal waste incineration, other
 183 waste combustion, electrical and measuring equipment, chemicals manufacturing, caustic soda
 184 production, and dental) were projected in aggregate. Silver mining was not included in this work
 185 because emissions from 2010 onwards are expected to be zero.

186 The change in activity levels in the future, A_t/A_{2010} , reflects the growth or shrinkage in activity
 187 for a particular source type, in a particular region, under a particular scenario. Some may grow,
 188 some may decline, depending on the influence of the world economy in general and the pressure
 189 of the climate change scenario. For example, coal combustion may increase under a lax climate
 190 scenario or decline under a stringent one. But A_t/A_{2010} only characterizes the change in the size of
 191 the source type, it says nothing about the transformation of it over the time period in question.
 192 New, high-performing technologies will undoubtedly replace older, low-performing ones; and
 193 the imposition of new emission control regulations may or may not force the use of add-on
 194 emission control technologies or even a complete change in production technology. All of these
 195 will influence Hg emissions. Except for Carbon Capture and Storage (CCS) and inferences from
 196 SO₂ emissions, the SSP scenarios say nothing about technology transformation that will
 197 influence Hg emissions. This, therefore, is the most challenging aspect of forecasting future Hg
 198 emissions. Our approach was to develop the ratio $EF_{t,r,s,f}/EF_{2010,r,s,f}$ as an indicator of how future
 199 emission rates will decline from their 2010 values. Note that this ratio is never greater than one
 200 (i.e., future emission rates are never higher in the future than in 2010 per unit of activity).

201 In previous work, we developed a methodology for estimating the time-development of emission
 202 factors for historical periods (pre-2010) using transformed normal distribution functions (Streets

203 et al., 2011). These region-specific functions were parameterized based on a detailed review of
204 experimental measurements around the world, as illustrated in that paper for copper smelting. It
205 was shown, for example, that the Hg emission rate for copper smelters pre-1900 was an
206 uncontrolled value of 27.5 gHg/MgCu worldwide. After 1900, emission rates declined, along
207 different pathways in different parts of the world, reaching values in 2010 ranging from a low of
208 0.60 gHg/MgCu in western Europe to a high of 11.6 gHg/MgCu in Africa.

209 The challenge in this work was to reasonably represent the continuation of historical *EF* trends
210 out beyond 2010 in the absence of guidance from the SSP forecasts. In this work, we focused on
211 the period 2010–2100, where technology transformation will have the biggest effect. For each of
212 the 11 key source types mentioned above, we assumed that by 2100 the emission rates in every
213 world region will have declined from their 2010 levels to the present-day emission rate of the
214 lowest-emitting region. Thus, in the case of copper smelting, all regions emit at 0.60 gHg/MgCu
215 by 2100, though the trajectories to reach it vary by region. This 2100 rate then continues for all
216 years beyond 2100. Intermediate decadal years in *EF* were determined as linear trends.

217 For the purposes of atmospheric modeling, speciation of these future atmospheric Hg emissions
218 into elemental Hg (Hg^0) and divalent Hg compounds (Hg^{II}) was determined in a similar way, by
219 extrapolation of the speciation splits in each region in the year 2010. These range rather widely,
220 from a high value of the Hg^0/Hg ratio of 0.88 in South America to a low of 0.25 in western
221 Europe. This reflects the different emission characteristics of, for example, mining in South
222 America and industrial manufacturing/well-controlled coal combustion in western Europe. As
223 time goes on it can be expected that the Hg^0/Hg ratio will decline everywhere, as artisanal and
224 small-scale mining techniques (with high Hg^0 emission rates) are retired, and industrial processes
225 and combustion become increasingly well controlled, leading to conversion of elemental Hg to
226 collectable, oxidized Hg compounds. In this work, we assumed that the 2010 ratios in high-
227 emitting regions approach the western European level or the North American level (0.33) by
228 2100, eventually leveling out at a technology-limiting value of 0.2 everywhere. Slight variations
229 were applied among the four scenarios to reflect anticipated patterns of future technology
230 transformations.

231 Finally, future releases of Hg to land and water were estimated following the method of Streets
232 et al. (2017, 2019a). In essence, this involves subtracting the air emissions from the total Hg
233 contained in the raw material that is processed. It was not possible to determine *a priori* the fate
234 of these releases by source type, technology level, or world region. Uncertainties in the few
235 quantitative estimates that have been made and the vast quantity of unknown factors for sources
236 in remote parts of the world essentially rule this out.

237 2.3 Global Atmospheric Hg Deposition

238 We used the GEOS-Chem global chemical transport model to simulate the atmospheric fate and
239 deposition of mercury emissions under each emissions scenario. The model version (12.8) used
240 here included detailed multi-phase oxidation of elemental Hg and gas-phase photolysis of
241 oxidized Hg species from Shah et al. (2021). Simulations were run using 2014–2019 MERRA-2
242 meteorology (Gelaro et al., 2017) on a 2×2.5 -degree horizontal grid with a 72-layer vertical
243 domain extending through the top of the stratosphere. The first two years of each simulation

244 were used for initialization and the final three years were averaged for analysis to reduce the
245 effects of meteorological variability on simulated deposition patterns.

246 We conducted 5-year simulations for each decade from 2020-2100 for each scenario in addition
247 to a common baseline scenario for the 2010 emission year. We hold meteorology constant across
248 decadal snapshots to isolate the effects of variation in future emissions. Emissions from the
249 seven world regions were distributed onto a 0.25×0.25 -degree grid based on the spatial
250 distributions established in prior work (Steenhuisen & Wilson, 2019). Relative fractions of North
251 American emissions from Canada, the United States, and Central America were scaled to reflect
252 2015 values reported in Streets et al. (2019b) for consistency with past work.

253 We constructed source-receptor functions to quantify changes in atmospheric Hg deposition
254 resulting from shifts in terrestrial and oceanic Hg^0 evasion and for each anthropogenic emission
255 region. Following Corbitt et al. (2011), we define each source-receptor function F_{ij} as:

$$F_{ij} = \frac{D_{ij}}{E_i} \#(2)$$

256 where D_{ij} is the total mercury deposition flux to receptor grid cell j from emissions in region i ,
257 and E_i is the magnitude of emissions from region i .

258 2.4 Global Biogeochemical Box Model (GBBM)

259 An updated version of the multi-compartment Global Biogeochemical Box Model (GBBM)
260 developed by Amos et al. (2013; 2014) was used to simulate future shifts in atmospheric
261 deposition from legacy mercury emissions (Text S1; Table S1-S2). The GBBM represents Hg
262 cycling between the atmosphere, terrestrial biosphere (fast, slow, protected), ocean (surface,
263 intermediate, deep), and removal by burial in marine sediment.

264 We added four new compartments to the GBBM that represent waste reservoirs (fast, slow,
265 protected, and immobilized) to explicitly track the fate of the estimated 1.13 Tg Hg released by
266 humans to land and water from 1510-2010 (Streets et al., 2019a). These releases included
267 tailings and waste from mining and metals production, chlor-alkali plants, and substantial
268 contributions from Hg use in commercial products (Horowitz et al., 2014; Streets et al., 2011). In
269 prior work, anthropogenic releases to land and water were added to soil compartments of the
270 GBBM (Streets et al., 2017). However, it is likely that the majority of such releases are
271 sequestered at contaminated sites and do not have the same diffuse impacts on deposition as
272 atmospheric sources (Guerrero & Schneider, 2023; Kocman et al., 2017). Therefore, we
273 independently tracked land and water Hg releases. We parameterized re-emissions of Hg^0 and
274 discharges of Hg^{II} to rivers from waste compartments using the same rate coefficients as for the
275 fast, slow, and protected terrestrial Hg in the GBBM. Land and water Hg releases were
276 partitioned into waste pools following the methods described in Streets et al. (2017) (Text S1).

277 We simulated the time-dependent fate of future anthropogenic Hg releases separately for each
278 scenario. In each simulation, the model was initialized by calculating the steady state distribution
279 of mercury among reservoirs under a constant geogenic Hg flux of 230 Mg a^{-1} from subaerial
280 volcanism and 50 Mg a^{-1} from hydrothermal vents (Geyman et al., 2023). The model was then

281 forced with all-time (2000 BCE to 2010 CE) anthropogenic mercury releases from Streets et al.
282 (2019) followed by emissions specified in each scenario from 2010-2300. Evaluation of model
283 results for the year 2010 agree with the observational ranges for the atmospheric Hg reservoir,
284 seawater concentrations, and atmospheric deposition enrichment factors (Table S3, Amos et al.,
285 2015).

286 **3 Results and Discussion**

287 3.1 Future Emission Trends

288 3.1.1 Long-term perspective on anthropogenic Hg releases

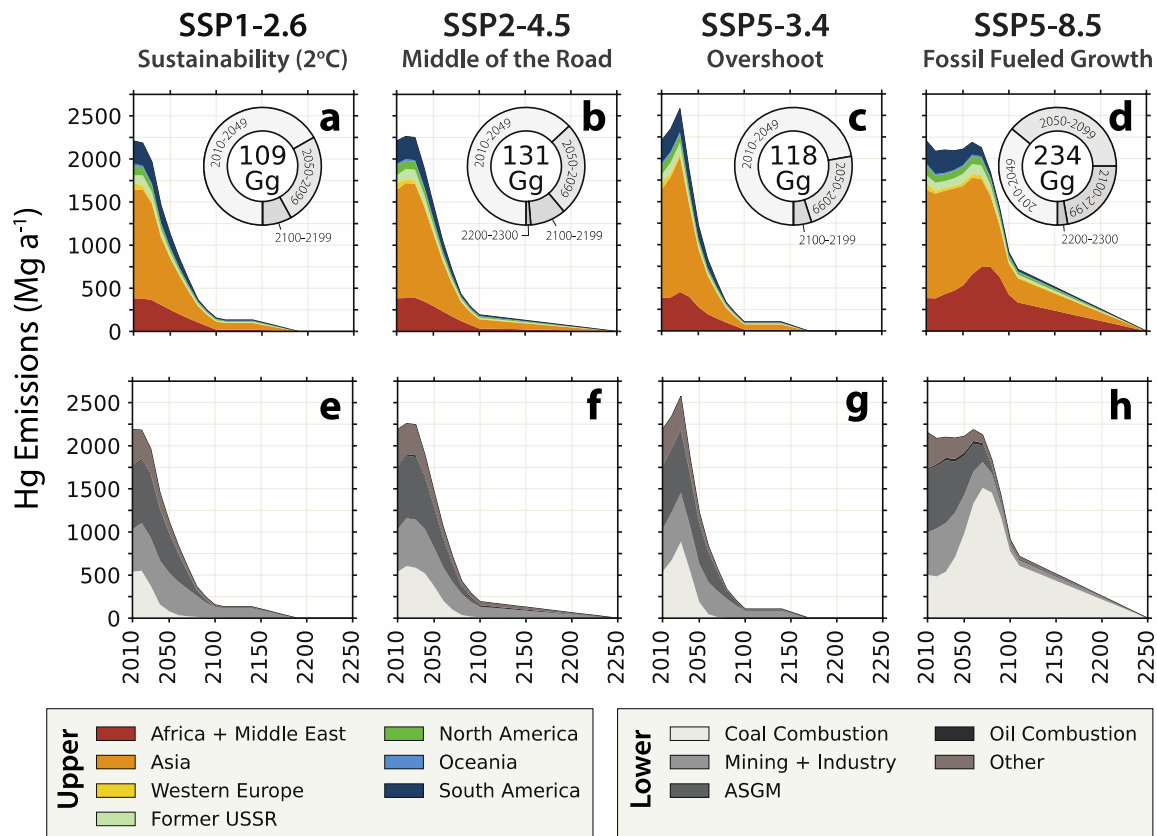
289 Atmospheric Hg emissions are shown by region (Fig. 1; Table S4) and source sector (Table S5)
290 for each of the four scenarios considered in this work. All primary Hg emissions are projected to
291 be zero beyond 2250, consistent with SSP assumptions. Projected cumulative Hg releases to air,
292 land, and water between 2010 and 2300 range from 709 Gg under SSP1-2.6, to 1710 Gg under
293 SSP5-8.5. Projected anthropogenic emissions between 2010 and 2300 are comparable to
294 cumulative historical emissions from 1510-2010 (1470 Gg) estimated in past work (Streets et al.,
295 2019a), suggesting human impacts on the global Hg cycle will be sustained for millennia.

296 Global Hg emissions projected in this work for the year 2050 are substantially lower than similar
297 forecasts made over a decade prior (2300-4900 Mg a⁻¹) using the IPCC SRES scenarios (Streets
298 et al., 2009). Projected anthropogenic emission declines for the year 2050 under SSP1-2.6 (-1080
299 Mg a⁻¹) are similar to those projected for 2035 by Pacyna et al. (2016) under a scenario involving
300 full implementation of policy commitments and plans made before 2016. Relative declines
301 projected in this work are partially attributable to lower Hg emission factors from recently
302 implemented Hg pollution controls (e.g., Zhang et al., 2023). Thus, lower future Hg emissions
303 estimated in this work reflect progress made through global policy efforts in recent decades.

304 Across all scenarios, future land and water Hg releases follow qualitatively similar trajectories to
305 atmospheric emissions. Land and water Hg releases grow as a fraction of total anthropogenic Hg
306 releases in the future. By 2100, anthropogenic Hg releases to land and water are estimated to be
307 12 to 25 times greater than anthropogenic Hg emissions to air, compared to only 3.3-fold greater
308 (7330 Mg a⁻¹) in 2010.

309

310



311
 312 **Figure 1. Global anthropogenic mercury (Hg) emissions to air by world region and source sector.**
 313 Trajectories under each scenario are shown by world region in Panels (a – d). Inset pie charts show fractional
 314 emissions occurring during four “snapshot” time periods, arranged clockwise from the bottom: 2010-2049,
 315 2050-2099, 2100-2200, 2200-2300. Cumulative emissions to air (Gg; 2010-2300) are shown in the center of
 316 each ring. Panels (e – f) provide a sector-specific breakdown of the same emission. ASGM = artisanal and
 317 small-scale gold mining.

318 3.1.2 Scenario-specific patterns in primary anthropogenic Hg releases

319 Among scenarios considered in this work, SSP1-2.6 is a lower-bound greenhouse gas emissions
 320 case, and it is known as the “2°C scenario.” SSP1-2.6 is characterized by aggressive reductions
 321 in greenhouse gas emissions and a nameplate end-century radiative forcing of 2.6 W m^{-2}
 322 (Meinshausen et al., 2020). Projected future atmospheric Hg emissions decline continuously after
 323 2010 (Fig. 1). In 2010, Asia was the largest regional contributor (1260 Mg a^{-1} ; 57% of total) to
 324 global atmospheric emissions (2190 Mg a^{-1}). Under SSP1-2.6, a 93% reduction in global Hg
 325 emissions is projected (154 Mg a^{-1}) by the year 2100, and Asia remains the largest remaining
 326 regional emitter (91 Mg a^{-1} , 59%). Beyond 2100, emissions continue to decline at a slower pace
 327 and reach zero by 2190, in accordance with SSP assumptions.

328 SSP2-4.5 is a middle-of-the-road scenario that reflects moderate socioeconomic, energy, and
 329 climate mitigation changes and a continuation of growth and development trajectories following
 330 the status quo (Meinshausen et al., 2020). Relative to 2010, Hg emissions grow slightly until

331 2030 and then decline at a rate similar to SSP1-2.6 (Fig. 1). Hg emissions are 193 Mg a^{-1} by
332 2100, which is only 25% greater than SSP1-2.6 (Fig. 1). SSP2-4.5 is not nearly as close to the
333 middle of the road for Hg emissions as it is for carbon emissions because it relies heavily on a
334 switch from coal to natural gas as the primary energy supply under moderate climate mitigation
335 efforts. This strategy results in continued greenhouse gas emissions and therefore results in
336 middle of the road climate effects. However, natural gas combustion generates insignificant
337 quantities of Hg, and so the trajectory is much lower. Hg emissions under SSP2-4.5 continue at a
338 low level into the distant future, eventually reaching zero in 2250 following SSP assumptions
339 (Fig. 1). Between 2010 and 2300, cumulative emissions to air are 131 Gg and cumulative
340 emissions to land and water are 737 Gg under SSP2-4.5.

341 SSP5-3.4 is the overshoot case characterized by a delay in climate-change action until after 2030,
342 leading to a major rise in Hg emissions between 2010 and 2030. Hg emissions are projected to
343 rise to 2580 Mg a^{-1} by 2030, an increase of 17% over 2010 (Fig. 1). Much of that growth occurs
344 in Asia. After 2030, emissions decline more precipitously than under the other three scenarios,
345 reaching levels similar to SSP1-2.6 by 2060. Hg emissions fall to 107 Mg a^{-1} by 2100 and reach
346 zero in the year 2170, which is earlier than SSP1-2.6. Under SSP5-3.4, cumulative emissions to
347 air are projected to be 118 Gg. Compared to SSP1-2.6, cumulative emissions are heavily
348 weighted toward the first few decades of the projection period. Cumulative emissions to land and
349 water are 618 Gg.

350 SSP5-8.5 is the upper-bound case, characterized by continued fossil-fuel use and minimal
351 consideration of environmental sustainability. Under this scenario, CO_2 concentrations are
352 projected to reach levels greater than 2000 ppm by 2200 (Meinshausen et al., 2020). Such levels
353 have not occurred on Earth since before the onset of the modern Antarctic glaciation over 40
354 Mya (Rae et al., 2021), and are associated with temperatures 3.3°C to 5.7°C higher in 2100 than
355 during the early-industrial period (1850-1900) (IPCC, 2023). Emissions of Hg to air remain near
356 present levels until after 2060 and then decline to 914 Mg a^{-1} (5-9 times the other scenarios) by
357 the end of the 21st century. The dominant Hg emission regions are Asia, where emissions exceed
358 1000 Mg a^{-1} through 2070, and Africa and the Middle East, where emissions grow from 383 Mg
359 a^{-1} in 2010 to 744 Mg a^{-1} in 2080. Emissions decline slowly beyond 2100, remaining at high
360 levels into the 22nd century: 512 Mg a^{-1} in 2150 and 256 Mg a^{-1} in 2200 (Fig. 1). Emissions do
361 not reach zero until 2250. Cumulative Hg releases (2010-2300) are 235 Gg to air and 1.47 Tg to
362 land and water under SSP5-8.5.

363 Several indicators suggest that global anthropogenic Hg emissions are tracking below levels
364 described in the overshoot scenario (SSP5-3.4) since 2010. While existing emission inventories
365 report growth in global anthropogenic Hg emissions between 2010 and 2015 (Streets et al.,
366 2019b), domestic policies have prompted widespread installation of air pollution control devices
367 over the past decade in China (Zhang et al., 2023) and the United States (Dai et al., 2023).
368 Trends in Hg^0 concentration and isotopic composition from long-term monitoring sites in China
369 also show declines consistent with suggested reductions in regional anthropogenic emissions
370 (Wu et al., 2023).

371 3.1.3 Decoupling of Hg emissions and radiative forcing under low coal use scenarios

372 Among source sectors in 2010, artisanal and small-scale gold mining (ASGM) was the largest
373 global source of atmospheric emissions (727 Mg a⁻¹), followed by coal combustion (538 Mg a⁻¹)
374 and mining and industry (491 Mg a⁻¹). Large-scale (rather than ASGM) gold production was the
375 largest source of Hg released to land and water (1990 Mg a⁻¹), followed by ASGM (1090 Mg a⁻¹),
376 electrical and measurement equipment (1010 Mg a⁻¹), chemicals manufacturing (860 Mg a⁻¹),
377 and zinc smelting (670 Mg a⁻¹). Coal combustion accounted for a greater fraction of global
378 atmospheric emissions (25%) in 2010 compared to land and water releases (5%, 370 Mg a⁻¹).

379 Differences in anthropogenic Hg emissions to air principally reflect differences in coal
380 combustion across SSP scenarios. Hg emissions from coal combustion are projected to grow by
381 2.3 to 12.5% and peak in 2020 under SSPs 1-2.6 and 2-4.5 (Fig. 1). Near-term increases in Hg
382 emissions from coal combustion reach levels 65% higher than 2010 under SSP5-3.4. Hg
383 emissions decline thereafter for lower coal-use scenarios (SSPs 1-2.6, 2-4.5 and 5-3.4). By 2050,
384 they fall to a fraction of 2010 levels (15% under SSP1-2.6 and 69% under SSP2-4.5) and reach
385 zero before the end of the century. In contrast, coal combustion persists until 2250 under SSP5-
386 8.5. Coal-related Hg emissions under SSP5-8.5 reach 990 Mg a⁻¹ (96% higher than 2010) by
387 2070 and remain 44% higher than 2010 levels by the end of the century (Fig. 1).

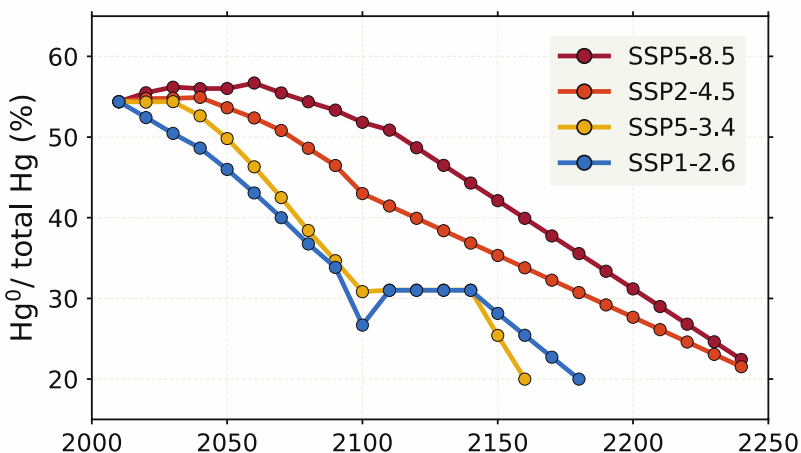
388 Among lower coal-use scenarios, coal combustion is responsible for 16 Gg (SSP1-2.6) to 28 Gg
389 (SSP2-4.5) of cumulative (2010-2300) Hg emissions to air. Cumulative Hg emissions to air from
390 coal combustion are ~5 to 9-fold greater under SSP5-8.5 (139 Gg) than the other scenarios, and
391 coal combustion comprises 59% of all emissions to air between 2010 and 2300 under SSP5-8.5.

392 Despite relative similarities in the phase-out of coal, SSPs 1-2.6, 2-4.5, and 5-3.4 show very
393 different greenhouse gas emission trajectories. Such differences arise from rates of natural gas
394 and oil combustion, as well as adoption of carbon capture and sequestration. These factors exert
395 minimal direct influence on primary anthropogenic Hg emissions, though they produce disparate
396 climate effects. For example, end-century surface temperatures simulated with the NASA GISS-
397 E2.1 climate model are 1.8°C – 2.3°C higher than the preindustrial (1850-1880) mean under
398 SSP1-2.6 compared to 2.7°C – 3.3°C under SSP2-4.5 (Nazarenko et al., 2022). The degree of
399 warming will modulate future changes in Hg emissions from the natural biosphere (e.g.,
400 Krabbenhoft & Sunderland, 2013; Schaefer et al., 2020). Therefore, it is important to consider
401 the consequences of human activity for both direct anthropogenic Hg releases and warming-
402 driven changes in Hg cycling in the biosphere and ocean (e.g., Schaefer et al., 2020; Schartup et
403 al., 2019).

404 3.1.4 Changes in Hg emission speciation favor local and regional deposition

405 The fraction of primary anthropogenic Hg emissions released to air as Hg⁰ is projected to decline
406 in the future (Fig. 2), with implications for transboundary pollution. For SSP1-2.6, the fraction of
407 Hg⁰ emitted by primary sources is projected to decline by 28% between 2010 and 2100. It
408 stabilizes from 2100-2140, and then declines continuously thereafter. By 2180, the last decade
409 with non-zero emissions for SSP1-2.6, Hg⁰ is projected to make up just 20% of total
410 anthropogenic Hg emissions to air (Fig. 2). Emission speciation under SSP5-3.4 broadly follows
411 that of SSP1-2.6, with slightly higher Hg⁰ fractions through 2100, and an accelerated decline
412 between 2140 and 2160 from 31% Hg⁰ to 20% Hg⁰ (Fig. 2). Under SSP2-4.5, Hg⁰ comprises a
413 larger fraction of total Hg emissions to air than under SSPs 1-2.6 and 5-3.4, remaining around

414 55% until 2040 (Fig. 2). The Hg^0 fraction then exhibits a slow decline with overall emissions and
 415 reaches 22% by 2240 (Fig. 2). SSP5-8.5 consistently represents an upper bound for the Hg^0
 416 fraction, increasing to 57% in 2060, followed by near-continuous declines to reach 22% by 2240.
 417 While trajectories vary across scenarios, greater fractions of Hg^{II} relative to Hg^0 in primary
 418 anthropogenic emissions are expected to produce future deposition patterns from primary
 419 emissions that increasingly reflect local and regional rather than global sources (Fig. S1).



420
 421 **Figure 2. Decadal changes in the speciation of primary anthropogenic mercury (Hg) emissions to air.**
 422 The percentage of total Hg emissions to air released as elemental Hg (Hg^0) is shown for each scenario and the
 423 remaining fraction consists of divalent mercury (Hg^{II}).

424 3.2. Future Deposition Patterns from Primary Anthropogenic Emissions

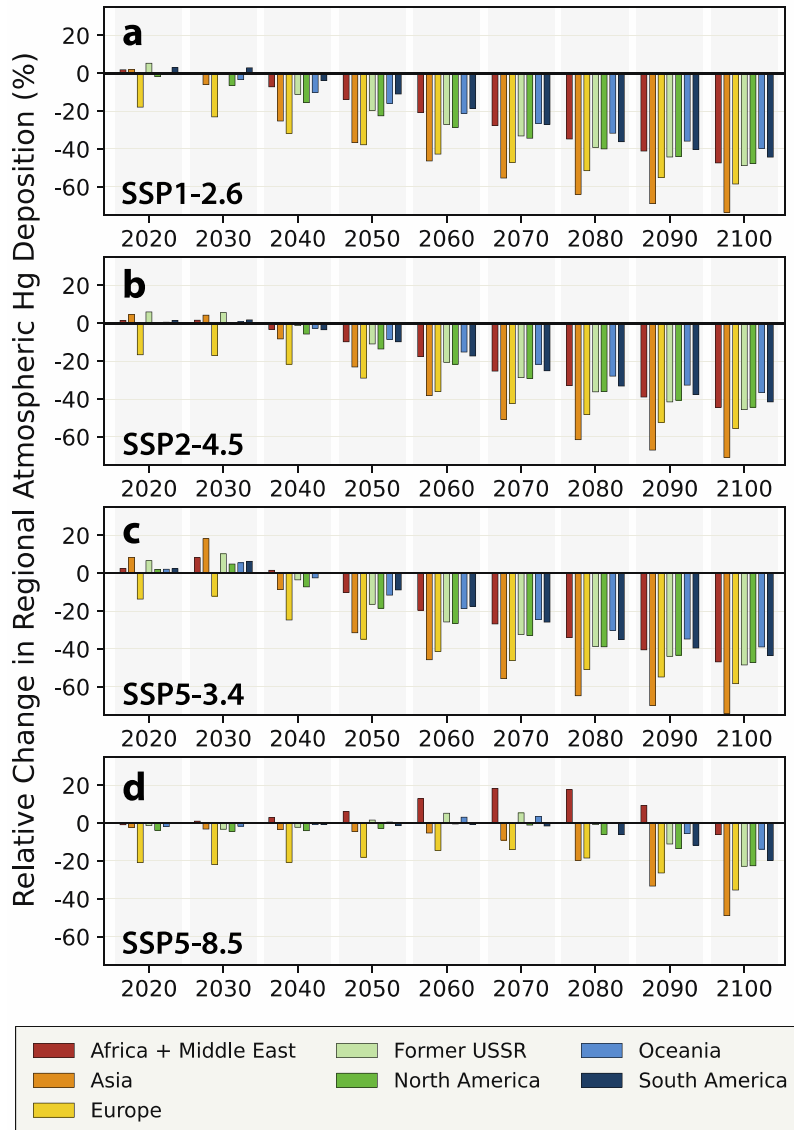
425 Modeled global Hg deposition to land increases by 22 Mg a^{-1} (0.9%) between 2010 and 2020
 426 under SSP1-2.6 emissions. This reflects increases from both primary anthropogenic emissions
 427 ($+8 \text{ Mg a}^{-1}$) and higher re-emissions from terrestrial and ocean surfaces due to increasing Hg
 428 reservoirs ($+14 \text{ Mg a}^{-1}$) (Fig. S2). Modeled increases in regional Hg deposition occur during this
 429 period over all global regions except for Europe and North America (Fig. 3a; 4a). There, declines
 430 in deposition from primary anthropogenic sources exceed increases in deposition from growing
 431 global terrestrial and oceanic Hg reservoirs and subsequent re-emissions. From 2040 through the
 432 end of the century, declines in atmospheric Hg deposition are projected for all regions. By 2100,
 433 total atmospheric Hg deposition is projected to be less than half of 2010 levels (46% , 1120 Mg a^{-1})
 434 (Fig. S2). The largest regional deposition declines are projected over Asia (-510 Mg a^{-1} ; $-$
 435 73%) because it was the largest source region in 2010 (Fig. 3a).

436 Temporal patterns in atmospheric Hg deposition under SSP2-4.5 are qualitatively similar to
 437 those of SSP1-2.6, characterized by slight but regionally heterogeneous near-term increases that
 438 give way to continuous decreases. Relative to 2010, global deposition increases by 1.7% in 2020
 439 and 1.6% in 2030. These increases occur over all regions except Europe, where declines are
 440 smaller than for SSP1-2.6 (-17% in 2020 and 2030) (Fig. 3b). By the end of the century,
 441 deposition to land is 1270 Mg a^{-1} lower than in 2010 (Fig. S2), with regional declines reaching
 442 71% ($-25 \mu\text{g m}^{-2} \text{ a}^{-1}$) in Asia (Fig. 3b).

443 Under SSP5-3.4, near-term deposition increases considerably, growing to 2690 Mg a⁻¹ (+9%) in
444 2030 over land (Fig. S2). The greatest increases occur in Asia, where total Hg deposition reaches
445 41 µg m⁻² a⁻¹ (+18%) in 2030. Deposition grows by greater than 8% over all regions except
446 Europe. After 2030, accelerated emission reductions relative to SSP1-2.6 result in comparable
447 end-century deposition, which is 1340 Mg a⁻¹ lower than in 2010 (Fig. S2).

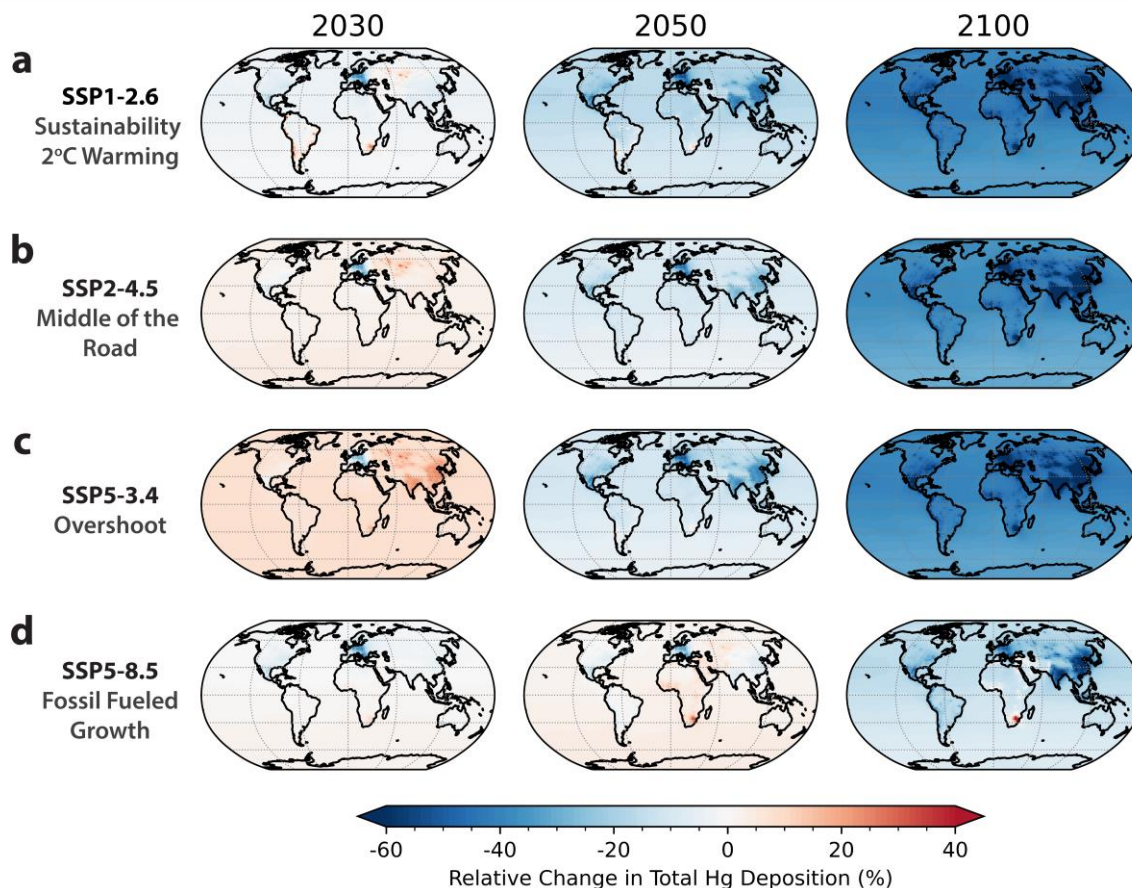
448 Atmospheric deposition under SSP5-8.5 is much higher than the other scenarios through most of
449 the century. However, 2020 deposition is the lowest of all scenarios, and 2030 deposition is
450 lower than all scenarios other than SSP1-2.6 (Fig. S2). Growth in emissions from Africa and the
451 Middle East, combined with sustained emissions elsewhere, produce increasing deposition over
452 most regions from 2020 until 2070. Most notably, deposition to Africa and the Middle East reach
453 levels 18% higher (+2.5 µg m⁻² a⁻¹) by 2070 and remain above baseline levels through 2100 (Fig.
454 3d; Fig. S2). End-century total deposition to land is 650 Mg a⁻¹ lower than in 2010.

455



456
457
458
459
460

Figure 3. Relative changes in regional atmospheric mercury (Hg) deposition compared to 2010. Changes in atmospheric Hg deposition are shown by world region (represented by colored bars) for each decade from 2020 to 2100 (x-axis). Each subplot represents temporal trends under a different Shared Socioeconomic Pathway (SSP) scenario (O'Neill et al., 2016).

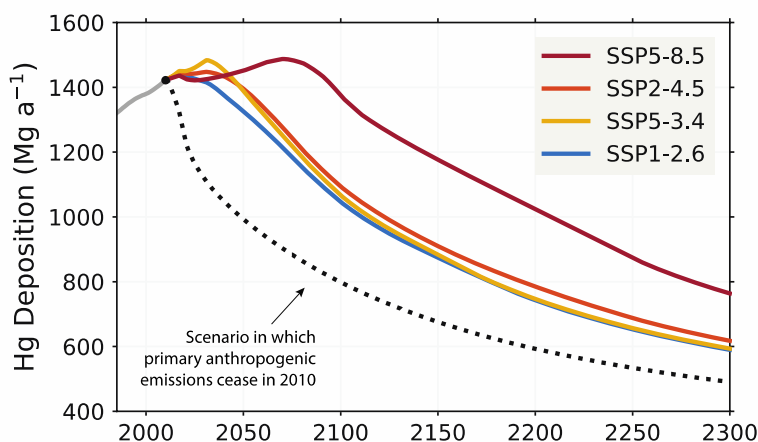


461
 462 **Figure 4. Trajectories of global atmospheric mercury (Hg) deposition.** Panels represent fractional change
 463 in total deposition relative to the 2010 baseline by scenario (rows) for three time periods: 2030 (left), 2050
 464 (center) and 2100 (right). Deposition is calculated as the sum of deposition from primary, legacy, and natural
 465 Hg emissions using the GEOS-Chem atmospheric mercury model (Shah et al., 2021) and the Global
 466 Biogeochemical Box Model (GBBM; Amos et al., 2013, 2014).

467 3.3 Implications for Legacy Hg Deposition from Terrestrial and Aquatic Emissions

468 Scenarios for deposition of legacy Hg vary among the four SSPs. Legacy deposition peaks
 469 before 2035 at levels 20 – 62 Mg a⁻¹ higher than 2010 under SSPs 1-2.6, 2-4.5, and 5-3.4 (Fig.
 470 5). Legacy deposition under SSP5-8.5 exhibits a larger and later peak, exceeding 2010 deposition
 471 by 66 Mg a⁻¹ in 2071 (Fig. 5). By 2100, relative trends in legacy deposition are notably different,
 472 with declines of 330 – 380 Mg a⁻¹ relative to 2010 for SSPs 1-2.6, 2-4.5 and 5-3.4, compared
 473 with a decline of 47 Mg a⁻¹ for SSP5-8.5 (Fig. 5). These end-century declines in legacy
 474 emissions are responsible for 26 – 28% of total declines in atmospheric Hg deposition to land
 475 under SSPs 1-2.6, 2-4.5, and 5-3.4, compared to 7% for SSP5-8.5.

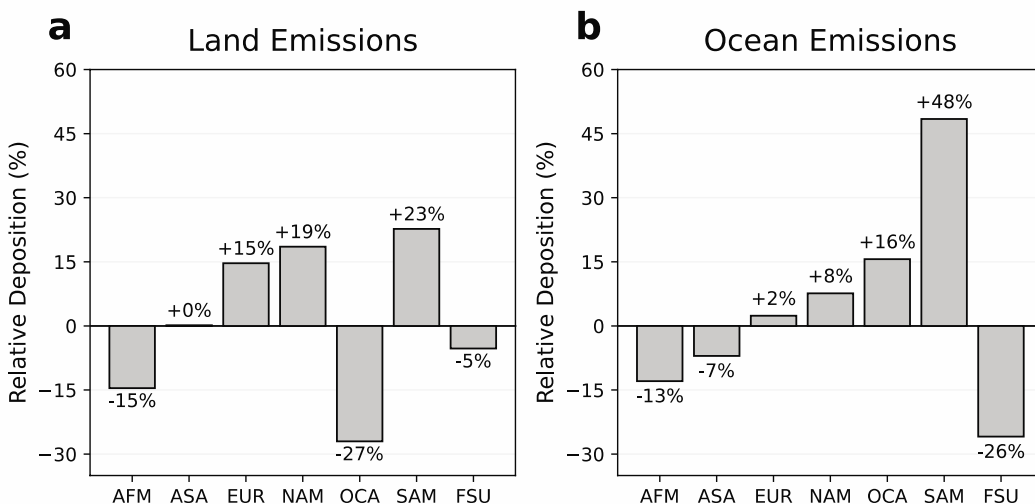
476



477
 478 **Figure 5. Mercury (Hg) deposition to land from legacy and natural emissions.** Trajectories under future
 479 emissions (2010-2300) are shown for SSPs 1-2.6 (blue line), 2-4.5 (orange line), 5-3.4 (yellow line), and 5-8.5
 480 (red line), in addition to a hypothetical scenario where primary anthropogenic emissions are zero after 2010
 481 (dotted black line). Implications of future trajectories for upper ocean reservoirs are shown in Figure S4.

482 Comparing SSPs 1-2.6 and 5-3.4 provides insights into the consequences of delaying emission
 483 reductions. Cumulative emissions through 2100 are comparable for SSP1-2.6 (101 Gg) and
 484 SSP5-3.4 (112 Gg). Additionally, anthropogenic Hg emissions are lower in 2100 under SSP5-3.4
 485 than SSP1-2.6 (107 Mg a⁻¹ and 154 Mg a⁻¹). Higher deposition to anthropogenic receptor regions
 486 in 2100 under SSP5-3.4 reflects a legacy deposition penalty for the unrestrained growth of the
 487 first three decades of the century. Deposition from legacy emissions is 20 Mg higher in 2100 for
 488 SSP5-3.4 compared to SSP1-2.6, whereas deposition from primary anthropogenic emissions is
 489 16 Mg lower. This example demonstrates the long-term benefits associated with near-term
 490 emissions mitigation, as discussed previously in Angot et al. (2018) and Amos et al. (2013).

491 By the end of the century, Hg re-emissions from the ocean and land will become relatively more
 492 important as sources of Hg deposition (Fig. S3), but deposition will not be evenly distributed by
 493 world region. Our source-receptor modeling suggests that South America receives the largest
 494 share of legacy Hg deposition on a per-area basis, receiving 23% higher deposition per unit of
 495 terrestrial emissions and 48% higher deposition per unit of ocean evasion than the area-weighted
 496 average of all world regions (Fig. 6). Such high rates of deposition over South America are
 497 driven by high rates of foliar uptake and wet deposition. In contrast, Oceania receives the lowest
 498 areal share of terrestrial emissions (73% of average), and the Former USSR receives the smallest
 499 areal share of Hg sourced from oceanic evasion (74% of average) (Fig. 6). Such low deposition
 500 is driven by the relative isolation of Oceania from terrestrial emissions and of the Former USSR
 501 from ocean emissions. These source-receptor relationships are subject to change in the future due
 502 to shifting patterns of historical anthropogenic Hg loading (e.g., Zolkos et al., 2022) and
 503 changing biogeochemical dynamics mediating deposition (e.g., Alexander & Mickley, 2015;
 504 Krabbenhoft & Sunderland, 2013; Yang et al., 2019).



505
 506 **Figure 6. Regional differences in area-normalized atmospheric Hg deposition from natural and legacy**
 507 **sources.** Bars represent differences in areal deposition rates between individual receptor regions and the
 508 average over land. Positive values mean that receptor regions receive greater deposition per unit area than
 509 average, and negative values mean that receptor regions receive less deposition than average. Individual panels
 510 show trends in deposition resulting from emissions from the terrestrial biosphere (a) and from the ocean (b).
 511 Receptor regions are Africa and the Middle East (AFM), Asia (ASA), Europe (EUR), North America (NAM),
 512 Oceania (OCA), South America (SAM), and the Former Soviet Union (FSU).

513 Globally averaged seawater Hg concentrations in the upper ocean (0-1500 m) are projected to
 514 increase over the coming decades across all scenarios in this study. The Hg reservoir in the upper
 515 ocean peaks at 142 to 151 Gg between 2037 (SSP1-2.6) and 2081 (SSP5-8.5) (Fig. S4). Near-
 516 term increases in upper ocean Hg concentrations are driven by future rather than historical
 517 emissions. Simulated seawater Hg concentrations begin declining in 2015 under a scenario with
 518 no future primary anthropogenic Hg releases (Fig. S4). By the end of the 21st century, upper
 519 ocean Hg concentrations are projected to be 15% lower than 2010 under SSP1-2.6 and are 11%
 520 higher than 2010 under SSP5-8.5.

521 4 Conclusions

522 The SSP scenarios evaluated in this work result in a greater than two-fold difference in
 523 cumulative anthropogenic Hg emissions between 2010 and 2300. Cumulative anthropogenic
 524 emissions to air and releases to land and water between 2010 and 2300 range from 710 Gg under
 525 the low-bound scenario (SSP1-2.6) to 1710 Gg under the upper-bound scenario (SSP5-8.5).
 526 These future releases are comparable to all-time historical anthropogenic emissions of 1540 Gg
 527 (80% CI: 1060 – 2800 Gg) (Streets et al., 2019a).

528 Transition of the energy sector away from coal combustion is the largest determinant of
 529 differences among scenarios, with lower bound and mid-range scenarios (SSPs 1-2.6, 2-4.5, 5-
 530 3.4) all exhibiting similar cumulative emissions due to declining coal usage. By contrast,
 531 industrial Hg mining and ASGM releases are projected to grow in relative importance in the
 532 future. These results imply that under the most stringent climate policies, the largest sources of
 533 Hg and CO₂ are likely to become more distinct from one another.

534 Numerous factors may affect regional Hg deposition patterns in the future. For most regions,
535 reducing primary anthropogenic Hg emissions remains the most effective way to reduce
536 deposition, since 55 – 71% of Hg^{II} emissions redeposit to the region of origin, compared to 5 –
537 13% for Hg⁰ (Fig. S5). However, the scenario-based trajectories described in this work indicate
538 that anthropogenic Hg^{II} emissions to air will decline more slowly than Hg⁰, causing Hg^{II} to grow
539 as a fraction of total anthropogenic Hg emissions to air. As the speciation of anthropogenic Hg
540 emissions shifts towards lower fractions of Hg⁰, a greater proportion of regional emissions will
541 redeposit to the region of origin. Across all regions, the fraction of self-sourced atmospheric Hg
542 deposition is projected to increase from 33% in 2010 to 35% – 45% in 2100 (Fig. S1).

543 Regional atmospheric Hg deposition patterns over the next century reflect trends in the
544 magnitude and spatial distribution of primary anthropogenic emissions as well as re-emissions
545 from the land and ocean. In regions where anthropogenic Hg emissions reductions are projected
546 to occur, total Hg deposition is expected to decrease, even during periods where global
547 deposition is increasing. This means that domestic policies have significant leverage on domestic
548 Hg deposition (e.g., Dai et al., 2023). However, greater reductions in anthropogenic emissions
549 are accompanied by larger declines in emissions from the land and ocean. Under SSP1-2.6, 28%
550 of the reduction in atmospheric deposition from 2010 to 2100 was the result of declines in legacy
551 emissions. As a result, globally-coordinated efforts to reduce near-term anthropogenic Hg
552 emissions will produce amplified benefits in terms of long-term declines in atmospheric
553 deposition (e.g., Angot et al., 2018).

554 **Acknowledgments**

555 Financial support for this work was provided by the U.S. National Science Foundation (award
556 numbers 2210173 and 2108452). The authors declare no competing financial interest. We thank
557 Zig Klimont of IIASA for providing the detailed activity and emissions datasets for the SSPs
558 used in this work.

559 **Open Research**

560 Mercury emission files, code and model output are available in an OSF repository (peer review
561 link provided with submission). The version of GEOS-Chem used in this study is available from
562 (<https://doi.org/10.5281/zenodo.3784796>).

563

564 **References**

- 565 Alexander, B., & Mickley, L. J. (2015). Paleo-Perspectives on Potential Future Changes in the Oxidative Capacity
566 of the Atmosphere Due to Climate Change and Anthropogenic Emissions. *Current Pollution Reports*, 1(2),
567 57–69. <https://doi.org/10.1007/s40726-015-0006-0>
- 568 Amos, H. M., Jacob, D. J., Streets, D. G., & Sunderland, E. M. (2013). Legacy impacts of all-time anthropogenic
569 emissions on the global mercury cycle. *Global Biogeochemical Cycles*, 27(2), 410–421.
570 <https://doi.org/10.1002/gbc.20040>
- 571 Amos, H. M., Jacob, D. J., Kocman, D., Horowitz, H. M., Zhang, Y., Dutkiewicz, S., et al. (2014). Global
572 Biogeochemical Implications of Mercury Discharges from Rivers and Sediment Burial. *Environmental*
573 *Science & Technology*, 48(16), 9514–9522. <https://doi.org/10.1021/es502134t>
- 574 Angot, H., Hoffman, N., Giang, A., Thackray, C. P., Hendricks, A. N., Urban, N. R., & Selin, N. E. (2018). Global
575 and Local Impacts of Delayed Mercury Mitigation Efforts. *Environmental Science and Technology*, 52(22),
576 12968–12977. <https://doi.org/10.1021/acs.est.8b04542>
- 577 Basu, N., Bastiansz, A., Dórea, J. G., Fujimura, M., Horvat, M., Shroff, E., et al. (2023). Our evolved understanding
578 of the human health risks of mercury. *Ambio*, 52(5), 877–896. <https://doi.org/10.1007/s13280-023-01831-6>
- 579 Corbitt, E. S., Jacob, D. J., Holmes, C. D., Streets, D. G., & Sunderland, E. M. (2011). Global source-receptor
580 relationships for mercury deposition under present-day and 2050 emissions scenarios. *Environmental*
581 *Science and Technology*, 45(24), 10477–10484. <https://doi.org/10.1021/es202496y>
- 582 Dai, M. Q., Geyman, B. M., Hu, X. C., Thackray, C. P., & Sunderland, E. M. (2023). Sociodemographic Disparities
583 in Mercury Exposure from United States Coal-Fired Power Plants. *Environmental Science & Technology*
584 *Letters*, 10(7), 589–595. <https://doi.org/10.1021/acs.estlett.3c00216>
- 585 Dellink, R., Chateau, J., Lanzi, E., & Magné, B. (2017). Long-term economic growth projections in the Shared
586 Socioeconomic Pathways. *Global Environmental Change*, 42, 200–214.
587 <https://doi.org/10.1016/j.gloenvcha.2015.06.004>
- 588 Fricko, O., Havlik, P., Rogelj, J., Klimont, Z., Gusti, M., Johnson, N., et al. (2017). The marker quantification of the
589 Shared Socioeconomic Pathway 2: A middle-of-the-road scenario for the 21st century. *Global*
590 *Environmental Change*, 42, 251–267. <https://doi.org/10.1016/j.gloenvcha.2016.06.004>
- 591 Gelaro, R., McCarty, W., Suárez, M. J., Todling, R., Molod, A., Takacs, L., et al. (2017). The modern-era
592 retrospective analysis for research and applications, version 2 (MERRA-2). *Journal of Climate*, 30(14),
593 5419–5454. <https://doi.org/10.1175/JCLI-D-16-0758.1>
- 594 Geyman, B. M., Thackray, C. P., Jacob, D. J., & Sunderland, E. M. (2023). Impacts of Volcanic Emissions on the
595 Global Biogeochemical Mercury Cycle: Insights from Satellite Observations and Chemical Transport
596 Modeling. *Geophysical Research Letters*, 50, e2023GRL104667. <https://doi.org/10.1029/2023GL104667>
- 597
- 598 Gidden, M. J., Riahi, K., Smith, S. J., Fujimori, S., Luderer, G., Kriegler, E., et al. (2019). Global emissions
599 pathways under different socioeconomic scenarios for use in CMIP6: a dataset of harmonized emissions
600 trajectories through the end of the century. *Geoscientific Model Development*, 12(4), 1443–1475.
601 <https://doi.org/10.5194/gmd-12-1443-2019>
- 602 Guerrero, S., & Schneider, L. (2023). The global roots of pre-1900 legacy mercury. *Proceedings of the National*
603 *Academy of Sciences*, 120(31), e2304059120. <https://doi.org/10.1073/pnas.2304059120>
- 604 Horowitz, H M, Jacob, D. J., Zhang, Y., Dibble, T. S., Slemr, F., Amos, H. M., et al. (2017). A new mechanism for
605 atmospheric mercury redox chemistry: implications for the global mercury budget. *Atmos. Chem. Phys.*,
606 17(10), 6353–6371. <https://doi.org/10.5194/acp-17-6353-2017>
- 607 Horowitz, Hannah M., Jacob, D. J., Amos, H. M., Streets, D. G., & Sunderland, E. M. (2014). Historical Mercury
608 Releases from Commercial Products: Global Environmental Implications. *Environmental Science &*
609 *Technology*, 48(17), 10242–10250. <https://doi.org/10.1021/es501337j>
- 610 Intergovernmental Panel on Climate Change (IPCC). (2023). Summary for Policymakers. In *Climate Change 2021 –*
611 *The Physical Science Basis: Working Group I Contribution to the Sixth Assessment Report of the*

- 612 *Intergovernmental Panel on Climate Change* (pp. 3–32). Cambridge: Cambridge University Press.
613 <https://doi.org/10.1017/9781009157896.001>
- 614 Jiang, L., & O'Neill, B. C. (2017). Global urbanization projections for the Shared Socioeconomic Pathways. *Global*
615 *Environmental Change*, 42, 193–199. <https://doi.org/10.1016/j.gloenvcha.2015.03.008>
- 616 Kc, S., & Lutz, W. (2017). The human core of the shared socioeconomic pathways: Population scenarios by age, sex
617 and level of education for all countries to 2100. *Global Environmental Change*, 42, 181–192.
618 <https://doi.org/10.1016/j.gloenvcha.2014.06.004>
- 619 Kocman, D., Wilson, S., Amos, H., Telmer, K., Steenhuisen, F., Sunderland, E., et al. (2017). Toward an
620 Assessment of the Global Inventory of Present-Day Mercury Releases to Freshwater Environments.
621 *International Journal of Environmental Research and Public Health*, 14(2), 138.
622 <https://doi.org/10.3390/ijerph14020138>
- 623 Krabbenhoft, D. P., & Sunderland, E. M. (2013). Global Change and Mercury. *Science*, 341(6153), 1457–1458.
624 <https://doi.org/10.1126/science.1242838>
- 625 Lund, M. T., Myhre, G., & Samset, B. H. (2019). Anthropogenic aerosol forcing under the Shared Socioeconomic
626 Pathways. *Atmospheric Chemistry and Physics*, 19(22), 13827–13839. [https://doi.org/10.5194/acp-19-](https://doi.org/10.5194/acp-19-13827-2019)
627 [13827-2019](https://doi.org/10.5194/acp-19-13827-2019)
- 628 Meinshausen, M., Nicholls, Z. R. J., Lewis, J., Gidden, M. J., Vogel, E., Freund, M., et al. (2020). The shared socio-
629 economic pathway (SSP) greenhouse gas concentrations and their extensions to 2500. *Geoscientific Model*
630 *Development*, 13(8), 3571–3605. <https://doi.org/10.5194/gmd-13-3571-2020>
- 631 Morfeldt, J., Nijs, W., & Silveira, S. (2015). The impact of climate targets on future steel production - An analysis
632 based on a global energy system model. *Journal of Cleaner Production*, 103, 469–482.
633 <https://doi.org/10.1016/j.jclepro.2014.04.045>
- 634 Myhre, G., Shindell, D., Bréon, F.-M., Collins, W., Fuglestedt, J., Huang, J., et al. (2013). Anthropogenic and
635 Natural Radiative Forcing. In T. F. Stocker, D. Qin, G.-K. Plattner, M. Tignor, S. K. Allen, J. Boschung, et
636 al. (Eds.), *Climate Change 2013: The Physical Science Basis. Contribution of Working Group I to the Fifth*
637 *Assessment Report of the Intergovernmental Panel on Climate Change*. Cambridge, United Kingdom and
638 New York, NY, USA: Cambridge University Press.
- 639 Nazarenko, L. S., Tausnev, N., Russell, G. L., Rind, D., Miller, R. L., Schmidt, G. A., et al. (2022). Future Climate
640 Change Under SSP Emission Scenarios With GISS-E2.1. *Journal of Advances in Modeling Earth Systems*,
641 14(7), e2021MS002871. <https://doi.org/10.1029/2021MS002871>
- 642 Nriagu, J. O. (1994). Mercury pollution from the past mining of gold and silver in the Americas. *Science of The*
643 *Total Environment*, 149(3), 167–181. [https://doi.org/10.1016/0048-9697\(94\)90177-5](https://doi.org/10.1016/0048-9697(94)90177-5)
- 644 O'Neill, B. C., Tebaldi, C., van Vuuren, D. P., Eyring, V., Friedlingstein, P., Hurtt, G., et al. (2016). The Scenario
645 Model Intercomparison Project (ScenarioMIP) for CMIP6. *Geoscientific Model Development*, 9(9), 3461–
646 3482. <https://doi.org/10.5194/gmd-9-3461-2016>
- 647 O'Neill, B. C., Kriegler, E., Ebi, K. L., Kemp-Benedict, E., Riahi, K., Rothman, D. S., et al. (2017). The roads
648 ahead: Narratives for shared socioeconomic pathways describing world futures in the 21st century. *Global*
649 *Environmental Change*, 42, 169–180. <https://doi.org/10.1016/j.gloenvcha.2015.01.004>
- 650 Pacyna, J. M., Travníkov, O., Simone, F. D., Hedgecock, I. M., Sundseth, K., Pacyna, E. G., et al. (2016). Current
651 and future levels of mercury atmospheric pollution on a global scale. *Atmospheric Chemistry and Physics*,
652 16(19), 12495–12511. <https://doi.org/10.5194/acp-16-12495-2016>
- 653 Rae, J. W. B., Zhang, Y. G., Liu, X., Foster, G. L., Stoll, H. M., & Whiteford, R. D. M. (2021). Atmospheric CO₂
654 over the Past 66 Million Years from Marine Archives. *Annual Review of Earth and Planetary Sciences*,
655 49(1), 609–641. <https://doi.org/10.1146/annurev-earth-082420-063026>
- 656 Rao, S., Klimont, Z., Smith, S. J., Van Dingenen, R., Dentener, F., Bouwman, L., et al. (2017). Future air pollution
657 in the Shared Socio-economic Pathways. *Global Environmental Change*, 42, 346–358.
658 <https://doi.org/10.1016/j.gloenvcha.2016.05.012>

- 659 Riahi, K., van Vuuren, D. P., Kriegler, E., Edmonds, J., O'Neill, B. C., Fujimori, S., et al. (2017). The Shared
660 Socioeconomic Pathways and their energy, land use, and greenhouse gas emissions implications: An
661 overview. *Global Environmental Change*, *42*, 153–168. <https://doi.org/10.1016/j.gloenvcha.2016.05.009>
- 662 Schaefer, K., Elshorbany, Y., Jafarov, E., Schuster, P. F., Striegl, R. G., Wickland, K. P., & Sunderland, E. M.
663 (2020). Potential impacts of mercury released from thawing permafrost. *Nature Communications*, *11*(1),
664 4650. <https://doi.org/10.1038/s41467-020-18398-5>
- 665 Schartup, A. T., Thackray, C. P., Qureshi, A., Dassuncao, C., Gillespie, K., Hanke, A., & Sunderland, E. M. (2019).
666 Climate change and overfishing increase neurotoxicant in marine predators. *Nature*, *572*(7771), 648–650.
667 <https://doi.org/10.1038/s41586-019-1468-9>
- 668 Shah, V., Jacob, D. J., Thackray, C. P., Wang, X., Sunderland, E. M., Dibble, T. S., et al. (2021). Improved
669 Mechanistic Model of the Atmospheric Redox Chemistry of Mercury. *Environmental Science &*
670 *Technology*, *acs.est.1c03160*. <https://doi.org/10.1021/acs.est.1c03160>
- 671 Steenhuisen, F., & Wilson, S. J. (2019). Development and application of an updated geospatial distribution model
672 for gridding 2015 global mercury emissions. *Atmospheric Environment*, *211*(December 2018), 138–150.
673 <https://doi.org/10.1016/j.atmosenv.2019.05.003>
- 674 Streets, D. G., Zhang, Q., & Wu, Y. (2009). Projections of global mercury emissions in 2050. *Environmental*
675 *Science and Technology*, *43*(8), 2983–2988. <https://doi.org/10.1021/es802474j>
- 676 Streets, D. G., Devane, M. K., Lu, Z., Bond, T. C., Sunderland, E. M., & Jacob, D. J. (2011). All-time releases of
677 mercury to the atmosphere from human activities. *Environmental Science and Technology*, *45*(24), 10485–
678 10491. <https://doi.org/10.1021/es202765m>
- 679 Streets, D. G., Horowitz, H. M., Jacob, D. J., Lu, Z., Levin, L., ter Schure, A. F. H., & Sunderland, E. M. (2017).
680 Total Mercury Released to the Environment by Human Activities. *Environmental Science & Technology*,
681 *51*(11), 5969–5977. <https://doi.org/10.1021/acs.est.7b00451>
- 682 Streets, D. G., Horowitz, H. M., Lu, Z., Levin, L., Thackray, C. P., & Sunderland, E. M. (2019a). Five hundred
683 years of anthropogenic mercury: spatial and temporal release profiles*. *Environmental Research Letters*,
684 *14*(8), 084004. <https://doi.org/10.1088/1748-9326/ab281f>
- 685 Streets, D. G., Horowitz, H. M., Lu, Z., Levin, L., Thackray, C. P., & Sunderland, E. M. (2019b). Global and
686 regional trends in mercury emissions and concentrations, 2010–2015. *Atmospheric Environment*,
687 *201*(December 2018), 417–427. <https://doi.org/10.1016/j.atmosenv.2018.12.031>
- 688 Sverdrup, H., Koca, D., & Granath, C. (2012). Modelling the gold market, explaining the past and assessing the
689 physical and economical sustainability of future scenarios. *Proceedings of the 30th International*
690 *Conference of the System Dynamics Society*, 1–23.
- 691 Sverdrup, H. U., & Olafsdottir, A. H. (2020). System Dynamics Modelling of the Global Extraction, Supply, Price,
692 Reserves, Resources and Environmental Losses of Mercury. *Water, Air, and Soil Pollution*, *231*(8), 1–22.
693 <https://doi.org/10.1007/s11270-020-04757-x>
- 694 Sverdrup, H. U., Olafsdottir, A. H., & Ragnarsdottir, K. V. (2019). On the long-term sustainability of copper, zinc
695 and lead supply, using a system dynamics model. *Resources, Conservation and Recycling: X*, *4*, 100007.
696 <https://doi.org/10.1016/j.rcrx.2019.100007>
- 697 Turnock, S. T., Allen, R. J., Andrews, M., Bauer, S. E., Deushi, M., Emmons, L., et al. (2020). Historical and future
698 changes in air pollutants from CMIP6 models. *Atmospheric Chemistry and Physics*, *20*(23), 14547–14579.
699 <https://doi.org/10.5194/acp-20-14547-2020>
- 700 Watari, T., Nansai, K., Giurco, D., Nakajima, K., McLellan, B., & Helbig, C. (2020). Global Metal Use Targets in
701 Line with Climate Goals. *Environmental Science & Technology*, *54*(19), 12476–12483.
702 <https://doi.org/10.1021/acs.est.0c02471>
- 703 Watari, T., Nansai, K., & Nakajima, K. (2021). Major metals demand, supply, and environmental impacts to 2100:
704 A critical review. *Resources, Conservation and Recycling*, *164*, 105107.
705 <https://doi.org/10.1016/j.resconrec.2020.105107>
- 706 Wu, X., Fu, X., Zhang, H., Tang, K., Wang, X., Zhang, H., et al. (2023). Changes in Atmospheric Gaseous
707 Elemental Mercury Concentrations and Isotopic Compositions at Mt. Changbai During 2015–2021 and Mt.

- 708 Ailao During 2017–2021 in China. *Journal of Geophysical Research: Atmospheres*, 128(10),
709 e2022JD037749. <https://doi.org/10.1029/2022JD037749>
- 710 Yang, Y., Meng, L., Yanai, R. D., Montesdeoca, M., Templer, P. H., Asbjornsen, H., et al. (2019). Climate change
711 may alter mercury fluxes in northern hardwood forests. *Biogeochemistry*, 146(1), 1–16.
712 <https://doi.org/10.1007/s10533-019-00605-1>
- 713 Zhang, C. Y., Han, R., Yu, B., & Wei, Y. M. (2018). Accounting process-related CO2 emissions from global cement
714 production under Shared Socioeconomic Pathways. *Journal of Cleaner Production*, 184, 451–465.
715 <https://doi.org/10.1016/j.jclepro.2018.02.284>
- 716 Zhang, Y., Zhang, L., Cao, S., Liu, X., Jin, J., & Zhao, Y. (2023). Improved Anthropogenic Mercury Emission
717 Inventories for China from 1980 to 2020: Toward More Accurate Effectiveness Evaluation for the
718 Minamata Convention. *Environmental Science & Technology*, 57(23), 8660–8670.
719 <https://doi.org/10.1021/acs.est.3c01065>
- 720 Zolkos, S., Zhulidov, A. V., Gurtovaya, T. Yu., Gordeev, V. V., Berdnikov, S., Pavlova, N., et al. (2022).
721 Multidecadal declines in particulate mercury and sediment export from Russian rivers in the pan-Arctic
722 basin. *Proceedings of the National Academy of Sciences*, 119(14). <https://doi.org/10.1073/pnas.2119857119>
723

Supporting Information for: **Projecting Global Mercury Emissions and Deposition Under the Shared Socioeconomic Pathways**

Benjamin M. Geyman¹, Colin P. Thackray¹, David G. Streets¹, Christine L. Olson², Kevin Schaefer², and Elsie M. Sunderland^{1,3}

¹ Harvard John A. Paulson School of Engineering and Applied Sciences, Cambridge, MA 01238, USA.

² National Snow and Ice Data Center, Cooperative Institute for Research in Environmental Sciences, University of Colorado Boulder, Boulder, CO, USA

³ Department of Environmental Health, Harvard School of Public Health, Boston, Massachusetts 02115, USA.

Contents of this file

Text S1

Tables S1 to S5

Figure S1 to S5

Introduction

The supporting information contains 1 text section, 5 tables, and 5 figures.

- Text S1. Global Biogeochemical Box Model description [[p.2](#)]
- Table S1. Modern mercury reservoir magnitudes and fluxes [[p.3-4](#)]
- Table S2. Rate coefficients used in Global Biogeochemical Box Model [[p.5](#)]
- Table S3. Global Biogeochemical Box Model evaluation [[p.6](#)]
- Table S4. Emissions by region for the base year and key future years (Mg a^{-1}) [[p.7](#)]
- Table S5. Emissions by source type for the base year and key future years (Mg a^{-1}) [[p.8](#)]
- Figure S1. Trends in the fraction of anthropogenic emissions redepositing to region of origin [[p.9](#)]
- Figure S2. Trajectories of atmospheric mercury (Hg) deposition from primary anthropogenic and legacy + natural emissions [[p.10](#)]
- Figure S3. Change in atmospheric mercury (Hg) deposition from legacy emissions, 2010-2100 [[p.11](#)]
- Figure S4. Scenario-specific mass trajectories of mercury (Hg) in the upper ocean (0-1500 m) [[p.12](#)]
- Figure S5. Mercury source-receptor matrices, by species [[p.13](#)]

32 **Text S1. Global Biogeochemical Box Model Description**

33

34 We simulate the temporal evolution of mercury in eleven global compartments using a modified version
 35 of the geochemical box model described in Amos et al. (2013). Model compartments include the
 36 atmosphere (ATM), three ocean compartments delineated based on depth (surface: OCS, intermediate:
 37 OCI, and deep: OCD), and three compartments for terrestrial vegetation and soils delineated based on
 38 organic carbon turnover time (fast: TF, slow: TS, and protected: TP).

39

40 We added four waste compartments to the existing model to track the fate of anthropogenic Hg
 41 emissions to land and water. Waste compartments are delineated based on turnover time in a manner
 42 analogous to terrestrial compartments, and are defined as fast (WF), slow (WS), protected (WP), and
 43 immobilized (WI). Model code is implemented in python and will be made available in a public
 44 repository upon publication.

45

46 Following Amos et al. (2013), the model is defined as a system of first-order differential equations:

47

$$48 \quad \frac{dm}{dt} = \mathbf{K}m + s$$

49

50 In which m is a vector containing the mass in each of the seven reservoirs, s is a vector containing inputs
 51 to each reservoir and \mathbf{K} is the 11 x 11 matrix of rate coefficients between each reservoir pair. We
 52 simulate the pre-anthropogenic natural steady state by solving $dm/dt = 0$ under a constant geogenic
 53 source of 230 Mg Hg a⁻¹ to the atmosphere (Geyman et al., 2023) and 50 Mg a⁻¹ to the deep ocean,
 54 reflecting the central estimate from Lamborg et al. (2006).

55

56 We construct \mathbf{K} using values adapted from Amos et al. (2014). We updated the atmospheric budget for
 57 consistency with the most recent GEOS-Chem simulation from Shah et al. (2021). We adjusted setting
 58 fluxes associated with marine particles in the ocean based on more recent measurements of Hg
 59 partitioning to particles (Cui et al., 2021; Lamborg et al., 2016).

60

61 We force the model with historical anthropogenic emissions (1510-2010) from Streets et al. (2019)
 62 followed by projected future emissions under each SSP scenario. Cumulative historical emissions are 345
 63 Gg Hg to the atmosphere, and 1127 Gg Hg to land and water. Land and water releases are categorized as
 64 mining (810 Gg) or non-mining (326 Gg). In each simulation year (t), the input vector, $s(t)$, was updated
 65 to contain both geogenic sources and anthropogenic emissions.

66

67 Mining releases to land/water were allocated to terrestrial reservoirs, with 5% to the slow pool and 95%
 68 to the armored pool. All other releases followed the parameterization described in Streets et al. (2017)
 69 with 40% assumed to be sequestered and considered unavailable for active cycling. The remaining 60%
 70 was allocated among the new fast, slow and protected waste pools according to the relative carbon
 71 distribution in the analogous soil pools from the Global Terrestrial Mercury Model (Smith-Downey et al.,
 72 2010). Anthropogenic release magnitudes are linearly interpolated from the original decadal time
 73 resolution for use in the model.

74

75 **Table S1. Present-day reservoirs and fluxes used to calculate first-order rate coefficients in**
 76 **11-box model of Hg global biogeochemical cycling.**

	Flux (Mg a⁻¹)
Atmosphere (ATM): 4.0 Gg^a	
Hg ^{II} deposition to ocean	3900 ^a
Hg ⁰ uptake by ocean, gross	2000 ^a
Hg ^{II} deposition to land	1600 ^a
Hg ⁰ deposition to land	1200 ^a
Surface Ocean (OCS): 2.9 Gg^b	
Hg ⁰ gross evasion to the atmosphere	4800 ^a
Hg ⁰ net evasion	2800 ^a
Particle settling to intermediate ocean	3300 ^b
Gross detrainment flux to intermediate ocean	5100 ^b
Intermediate Ocean (OCI): 130 Gg^c	
Particle settling to deep ocean	600
Upwelling intermediate to surface	7100 ^c
Downwelling intermediate to deep	340 ^c
Deep Ocean (OCD): 220 Gg^c	
Particle settling; burial to deep sediment	210 ^c
Upwelling deep to intermediate	180 ^c
Fast Terrestrial (TF): 9.6 Gg^d	
Evasion due to heterotrophic respiration of SOM	40 ^e
Photoreduction	80 ^e
Biomass burning; fast to atmosphere	290 ^f
Riverine export to surface ocean	110 ^g
Riverine export to continental margin sediment	600 ^g
Decomposition; fast to slow	330 ^d
Decomposition and mineral stabilization; fast to protected	10 ^d
Slow Soil (TS): 35 Gg^d	
Evasion due to heterotrophic respiration of SOM	20 ^e
Biomass burning; slow to atmosphere	8 ^f
Riverine export to surface ocean	3 ^g
Riverine export to continental margin sediment	17 ^g
Decomposition; slow to fast*	210 ^d
Decomposition and mineral stabilization; slow to protected	0.5 ^d
Protected Soil (TP): 190 Gg^{d,**}	
Evasion due to heterotrophic respiration of SOM	3 ^e
Biomass burning; protected to atmosphere	4 ^f
Riverine export to surface ocean	2 ^g
Riverine export to continental margin sediment	10 ^g
Decomposition; protected to fast*	20 ^d
External Inputs	
Subaerial volcanism emissions to atmosphere	230 ^h
Submarine volcanism emissions to deep ocean	50 ⁱ
Anthropogenic emissions to air, land, water	$f(t)^j$

77 First-order rate coefficients, k , are calculated as $k_{ij} = F_{ij}/m_i$, where F_{ij} and m_i are the fluxes (Mg a⁻¹) and reservoir sizes (Gg)
 78 provided in the table above.

79 ^aShah et al. (2021)

80 ^bSoerensen et al. (2010)

81 ^cSunderland & Mason (2007)

82 ^dSmith-Downey et al. (2010)

83 ^eAmos et al. (2014). Values reflect downward revision of terrestrial evasion fluxes relative to Smith-Downey et al. (2010) based
 84 on observations and empirical models suggesting greater retention of deposited Hg than previous estimates (Hararuk et al.,
 85 2013; Obrist, 2012; Obrist et al., 2014).

86 ^fTotal biomass burning is 300 Mg a⁻¹ (Holmes et al., 2010) of which 95% is estimated to come from vegetation and 5% from the
 87 soil pools based on their carbon content (Smith-Downey et al., 2010).

88 ^gBased on present-day "background" global river discharge to terrestrial margin of 740 Mg a⁻¹ from Amos et al. (2014), and
 89 assumption that 16% of riverine reaches open ocean based on estimate that all dissolved riverine Hg reaches the open ocean
 90 (9% of total) and 6-7% of particulate riverine Hg reaches the open ocean (Zhang et al., 2015). Riverine Hg not reaching the open

91 ocean is buried in continental margin sediment. Riverine Hg fluxes are sourced from terrestrial pools in the same manner as
92 biomass burning, with 95% is estimated to come from vegetation and 5% from the soil pools based on their carbon content
93 (Smith-Downey et al., 2010).

94 ^h Geyman et al. (2023)

95 ⁱ Lamborg et al., (2006)

96 ^j Function of time; see Methods in main text and Text S1 for more details.

97 * Transfer of soil Hg from longer-lived to shorter-lived reservoirs represents processes such as priming and changes in the
98 degree of mineral stabilization of soil organic matter.

99 ** Soil Hg reservoirs are based on global estimates made for organic soils using the Global Terrestrial Mercury Model (GTMM;
100 Smith-Downey et al., 2010), a mechanistic global model facilitating self-consistent internal transfer and external Hg fluxes for
101 the terrestrial biosphere. Large-scale geochemical soil survey results suggest greater total Hg mass in global topsoil than in the
102 GTMM (Ballabio et al., 2021; Olson et al., 2022), but more work is needed to understand the implications of these findings for
103 the terrestrial Hg budget.

104

105 **Table S2. Rate coefficients used in global biogeochemical box model.**

Compartment From (<i>i</i>)	Compartment To (<i>j</i>)	Rate (a^{-1})*
Atmosphere	Terrestrial Fast	5.00×10^{-1}
	Terrestrial Slow	1.28×10^{-1}
	Terrestrial Protected	7.20×10^{-2}
	Ocean Surface	1.47×10^0
Terrestrial Fast	Atmosphere	4.36×10^{-2}
	Terrestrial Slow	3.44×10^{-2}
	Terrestrial Protected	1.04×10^{-3}
	Ocean Surface	1.24×10^{-2}
	Margin Sediment Burial	6.16×10^{-2}
Terrestrial Slow	Atmosphere	9.43×10^{-4}
	Terrestrial Fast	6.00×10^{-3}
	Terrestrial Protected	1.43×10^{-5}
	Ocean Surface	8.97×10^{-5}
	Margin Sediment Burial	4.45×10^{-4}
Terrestrial Protected	Atmosphere	3.68×10^{-5}
	Terrestrial Fast	7.89×10^{-5}
	Ocean Surface	9.01×10^{-6}
	Margin Sediment Burial	4.47×10^{-5}
Ocean Surface	Atmosphere	1.66×10^0
	Ocean Intermediate	2.90×10^0
Ocean Intermediate	Ocean Surface	5.46×10^{-2}
	Ocean Deep	7.23×10^{-3}
Ocean Deep	Ocean Intermediate	8.18×10^{-4}
	Marine Sediment Burial	9.55×10^{-4}
Waste Fast	Atmosphere	4.36×10^{-2}
	Terrestrial Slow	3.44×10^{-2}
	Terrestrial Protected	1.04×10^{-3}
	Ocean Surface	1.24×10^{-2}
	Margin Sediment Burial	6.16×10^{-2}
Waste Slow	Atmosphere	9.43×10^{-4}
	Terrestrial Fast	6.00×10^{-3}
	Terrestrial Protected	1.43×10^{-5}
	Ocean Surface	8.97×10^{-5}
	Margin Sediment Burial	4.45×10^{-4}
Waste Protected	Atmosphere	3.68×10^{-5}
	Terrestrial Fast	7.89×10^{-5}
	Ocean Surface	9.01×10^{-6}
	Margin Sediment Burial	4.47×10^{-5}

Compartment From (<i>i</i>)	Compartment To (<i>j</i>)	Rate (a^{-1})*
Waste Immobile	Atmosphere	1.00×10^{-20}

106 *Rates are calculated from the sum of fluxes in cases where mass transfer between a pair of reservoirs
107 (*i,j*) is composed of multiple fluxes.

108

109 **Table S3. Global Biogeochemical Box Model Evaluation**

Constraint Description	Model Value	Reference Value
Mass Hg in modern troposphere (Gg)	3.9	4.0 ^a
Upper ocean Hg concentration (0-1500 m) (pM)	1.2	0.8 – 1.8 ^b
Deep ocean (>1500m) Hg concentration (pM)	1.2	1.1 – 1.7 ^b
Pre-industrial to modern atmospheric Hg deposition enrichment factor (1840-20 th century maximum)	4.1	3 – 5 ^c

110 ^a Shah et al. (2021)111 ^b (Lamborg et al., 2014; Sunderland & Mason, 2007)112 ^c (Fitzgerald et al., 2005; Li et al., 2020; Sonke et al., 2023)

113 **Table S4. Mercury emissions by region for the base year and key future years (Mg a⁻¹)**

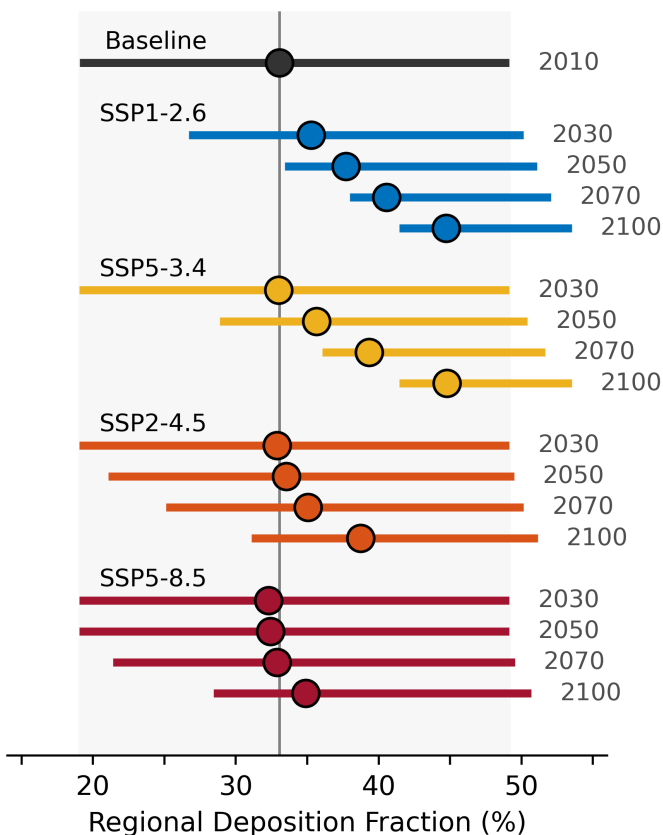
1-2.6	2010	2030	2050	2100	2150	2200	2250
NAM	109.3	79.4	44.8	12.8	8.8		
SAM	263.6	253.9	153.4	9.8	6.7		
EUR	85.7	30.7	16.7	7.0	4.8		
FSU	86.5	107.7	53.9	9.3	6.4		
AFM	383.2	363.4	251.1	21.1	14.5		
ASA	1255.5	1115.3	597.8	90.9	62.6		
OCA	25.6	15.3	8.3	3.5	2.4		
GLO	2209.4	1965.8	1126.0	154.3	106.3	0	0
2-4.5	2010	2030	2050	2100	2150	2200	2250
NAM	109.3	92.2	61.4	15.8	10.5	5.3	
SAM	263.6	261.0	159.9	13.4	8.9	4.5	
EUR	85.7	37.9	26.2	8.6	5.7	2.9	
FSU	86.5	124.2	74.8	11.1	7.4	3.7	
AFM	383.2	388.1	293.7	34.4	23.0	11.5	
ASA	1255.5	1325.3	841.0	104.9	69.9	35.0	
OCA	25.6	18.9	13.1	4.3	2.9	1.4	
GLO	2209.4	2247.7	1470.2	192.5	128.3	64.2	0
5-3.4	2010	2030	2050	2100	2150	2200	2250
NAM	109.3	99.8	44.7	9.5	6.3		
SAM	263.6	270.7	155.6	7.4	4.9		
EUR	85.7	41.8	16.5	5.2	3.5		
FSU	86.5	123.1	52.7	5.4	3.6		
AFM	383.2	452.0	278.3	17.3	11.5		
ASA	1255.5	1568.6	678.0	59.0	39.1		
OCA	25.6	20.9	8.2	2.6	1.7		
GLO	2209.4	2576.9	1234.0	106.6	70.6	0	0
5-8.5	2010	2030	2050	2100	2150	2200	2250
NAM	109.3	81.4	82.5	38.5	21.5	10.8	
SAM	263.6	264.7	184.7	31.4	17.6	8.8	
EUR	85.7	31.2	37.2	21.0	11.8	5.9	
FSU	86.5	80.9	103.7	33.4	18.7	9.3	
AFM	383.2	428.7	527.9	422.9	236.9	118.4	
ASA	1255.5	1198.8	1155.8	356.7	199.8	99.9	
OCA	25.6	15.6	18.6	10.5	5.9	2.9	
GLO	2209.4	2101.2	2110.3	914.3	512.1	256.1	0

114 **Region names:** NAM = North America, SAM = South America, EUR = Western Europe, FSU = Former
115 Soviet Union, AFM = Africa and the Middle East, ASA = Asia, OCA = Oceania.
116

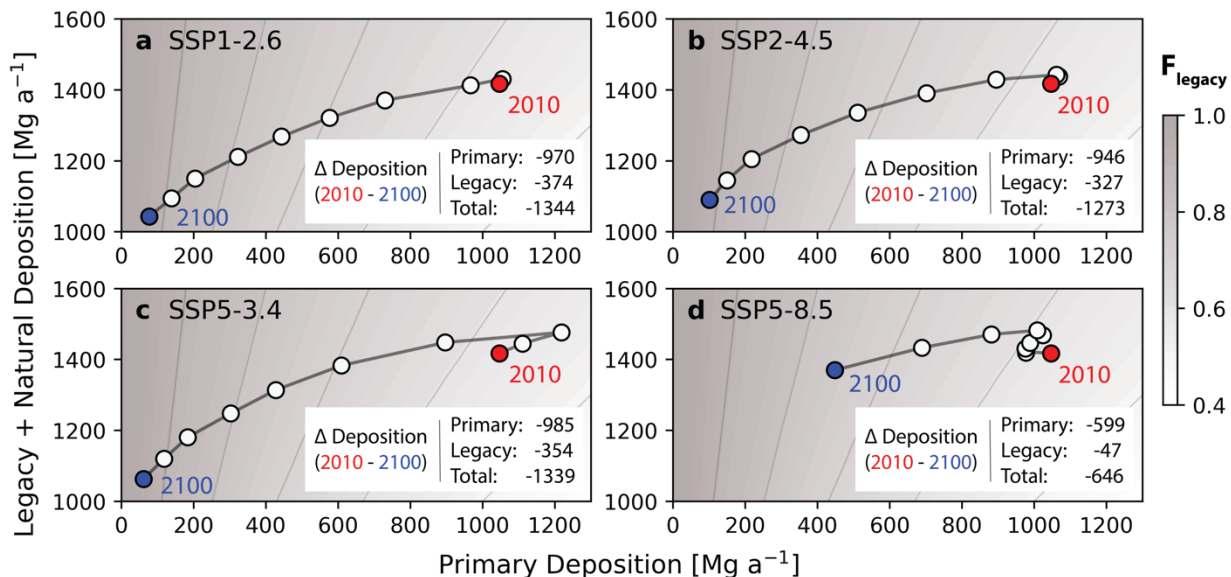
117 **Table S5. Mercury emissions by source category for the base year and key future years (Mg a⁻¹)**

1-2.6	2010	2030	2050	2100	2150	2200	2250
Mining and Industry	491.1	556.9	445.3	121.5	83.7		
Artisanal Gold Mining	726.8	726.8	457.3	0	0		
Coal Combustion	538.2	375.2	79.6	5.1	3.5		
Oil Combustion	14.5	17.1	13.0	3.7	2.5		
Other	438.9	289.8	130.8	24.1	16.6		
Total	2209.4	1965.8	1126.0	154.3	106.3	0	0
2-4.5	2010	2030	2050	2100	2150	2200	2250
Mining and Industry	491.1	556.9	445.3	121.5	81.0	40.5	
Artisanal Gold Mining	726.8	726.8	457.3	0	0	0	
Coal Combustion	538.2	584.7	372.0	10.9	7.3	3.6	
Oil Combustion	14.5	20.9	23.9	16.9	11.2	5.6	
Other	438.9	358.4	171.7	43.3	28.9	14.4	
Total	2209.4	2247.7	1470.2	192.5	128.3	64.2	0
5-3.4	2010	2030	2050	2100	2150	2200	2250
Mining and Industry	491.1	565.3	443.4	85.6	56.7		
Artisanal Gold Mining	726.8	726.8	457.3	0	0		
Coal Combustion	538.2	888.4	187.8	0.8	0.5		
Oil Combustion	14.5	18.4	22.7	7.4	4.9		
Other	438.9	378.0	122.8	12.8	8.5		
Total	2209.4	2576.9	1234.0	106.6	70.6	0	0
5-8.5	2010	2030	2050	2100	2150	2200	2250
Mining and Industry	491.1	565.3	443.4	85.6	48.0	24.0	
Artisanal Gold Mining	726.8	726.8	457.3	0	0	0	
Coal Combustion	538.2	539.6	985.8	775.3	434.2	217.1	
Oil Combustion	14.5	28.5	32.7	15.2	8.5	4.2	
Other	438.9	241.0	191.1	38.3	21.5	10.7	
Total	2209.4	2101.2	2110.3	914.3	512.1	256.1	0

118

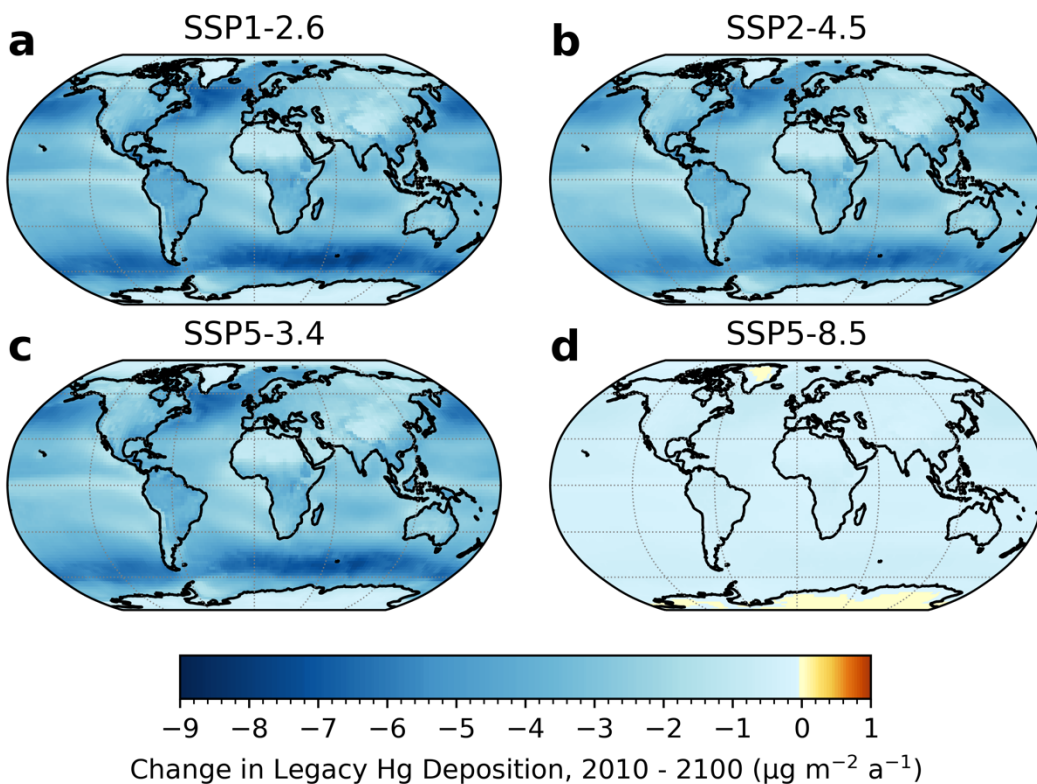


119
 120 **Figure S1. Trends in the fraction of anthropogenic emissions redepositing to region of origin.** Lines represent the
 121 range among individual world regions and points represent the fraction of total anthropogenic emissions that re-
 122 deposit to the region of origin. Values are separated by scenario (SSP1-2.6, SSP5-3.4, SSP2-4.5, SSP5-8.5) and
 123 presented for selected years (2030, 2050, 2070, 2100). Values for the baseline year (2010) are shown at the top of
 124 the figure in black, with the central value (vertical grey line) and regional range (grey shaded area) shown for
 125 comparison. Trends are driven by changes in the speciation of anthropogenic emissions. As the percentage of total
 126 Hg released as elemental Hg (Hg^0) declines in anthropogenic Hg emissions to air, the fraction of anthropogenic
 127 emissions redepositing to the region of origin increases. Note that the speciation of anthropogenic emissions
 128 continues to shift towards lower Hg^0 percentages beyond 2100 (Fig. 2).



129
 130 **Figure S2. Trajectories of atmospheric mercury (Hg) deposition from primary anthropogenic and legacy + natural**
 131 **emissions.** Changes in the emission drivers of deposition can be visualized over sequential decadal snapshots from
 132 2010 (blue) to 2100 (red). Deposition is calculated over ice-free land surfaces, with total deposition being the sum
 133 of deposition from legacy + natural emissions (y-axis) and deposition from primary anthropogenic emissions (x-
 134 axis). Panels a – d represent different Shared Socioeconomic Pathway (SSP) scenarios. The background of each
 135 panel is shaded to show the fraction of total deposition from legacy + natural sources. Inset annotations indicate
 136 the change in deposition between 2010 and 2100 for each category. Note that all temporal change in the “legacy +
 137 natural” deposition category is due to change in the legacy component because natural deposition is fixed.
 138

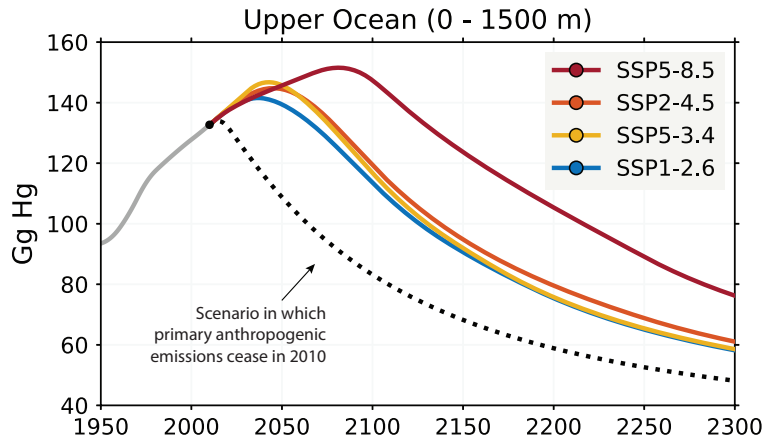
139



140

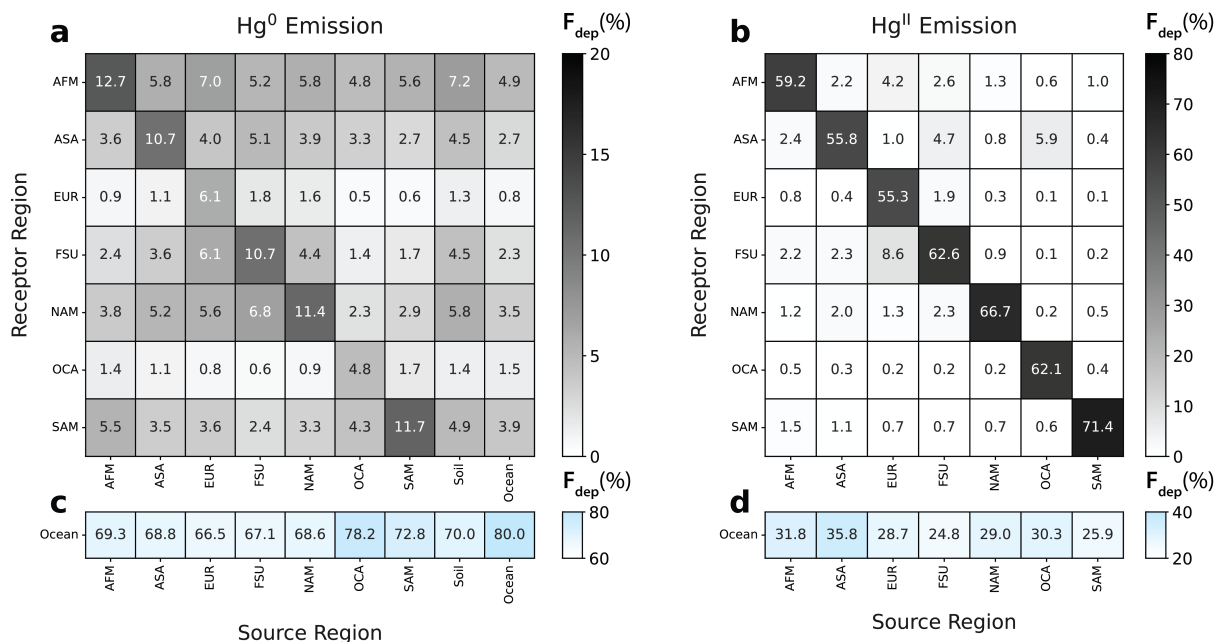
141

142 **Figure S3. Change in atmospheric mercury (Hg) deposition from legacy emissions, 2010-2100.** Patterns of
 143 deposition for 2010 and 2100 are calculated based on emissions from the ocean and terrestrial biosphere, which
 144 are quantified by forcing the global biogeochemical box model (GBBM) with historical (1510-2010) emissions from
 Streets et al. (2019) and scenario-specific future emissions. Emissions from the ocean and terrestrial biosphere
 145 include a “natural” component, though all change in the deposition shown here is attributable to change in legacy
 146 emissions because natural emissions are fixed. Deposition change is calculated as the difference between 2100
 147 and 2010 values.



148
149
150
151

Figure S4. Scenario-specific mass trajectories of mercury (Hg) in the upper ocean (0-1500 m). Trajectories under future emissions (2010-2300) are shown for SSPs 1-2.6 (blue), 2-4.5 (orange), 5-3.4 (yellow), and 5-8.5 (red), in addition to a reference scenario in which primary anthropogenic emissions cease in 2010 (dashed black).



152
 153 **Figure S5. Mercury source-receptor matrices, by species.** Matrix elements represent the fraction of a unit
 154 emission from a given source (column) to a given receptor (row). Source-receptor matrices are presented for
 155 emissions of gaseous elemental mercury (panels **a** and **c**) and gaseous oxidized mercury (panels **b** and **d**). Note that
 156 the sum down an entire column in (**a**, **c**) and (**b**, **d**) is close to, but not quite 1, resulting from a small fraction of
 157 deposition which occurs to global ice surfaces and a rapid re-emission process in the model. Also note the
 158 differences in color scale between species.
 159
 160

161 **References**

162

- 163 Amos, H. M., Jacob, D. J., Streets, D. G., & Sunderland, E. M. (2013). Legacy impacts of all-time anthropogenic
 164 emissions on the global mercury cycle. *Global Biogeochemical Cycles*, 27(2), 410–421.
 165 <https://doi.org/10.1002/gbc.20040>
- 166 Amos, H. M., Jacob, D. J., Kocman, D., Horowitz, H. M., Zhang, Y., Dutkiewicz, S., et al. (2014). Global
 167 Biogeochemical Implications of Mercury Discharges from Rivers and Sediment Burial. *Environmental*
 168 *Science & Technology*, 48(16), 9514–9522. <https://doi.org/10.1021/es502134t>
- 169 Ballabio, C., Jiskra, M., Osterwalder, S., Borrelli, P., Montanarella, L., & Panagos, P. (2021). A spatial assessment
 170 of mercury content in the European Union topsoil. *Science of the Total Environment*, 769, 144755.
 171 <https://doi.org/10.1016/j.scitotenv.2020.144755>
- 172 Cui, X., Lamborg, C. H., Hammerschmidt, C. R., Xiang, Y., & Lam, P. J. (2021). The Effect of Particle
 173 Composition and Concentration on the Partitioning Coefficient for Mercury in Three Ocean Basins.
 174 *Frontiers in Environmental Chemistry*, 2(May), 1–16. <https://doi.org/10.3389/fenvc.2021.660267>
- 175 Fitzgerald, W. F., Engstrom, D. R., Lamborg, C. H., Tseng, C. M., Balcom, P. H., & Hammerschmidt, C. R. (2005).
 176 Modern and historic atmospheric mercury fluxes in northern Alaska: Global sources and arctic depletion.
 177 *Environmental Science and Technology*, 39(2), 557–568. <https://doi.org/10.1021/es049128x>
- 178 Geyman, B. M., Thackray, C. P., Jacob, D. J., & Sunderland, E. M. (2023). Impacts of Volcanic Emissions on the
 179 Global Biogeochemical Mercury Cycle: Insights from Satellite Observations and Chemical Transport
 180 Modeling. *Geophysical Research Letters*, 50, e2023GRL104667. <https://doi.org/10.1029/2023GL104667>
- 181 Hararuk, O., Obrist, D., & Luo, Y. (2013). Modelling the sensitivity of soil mercury storage to climate-induced
 182 changes in soil carbon pools. *Biogeosciences*, 10(4), 2393–2407. <https://doi.org/10.5194/bg-10-2393-2013>
- 183 Holmes, C. D., Jacob, D. J., Corbitt, E. S., Mao, J., Yang, X., Talbot, R., & Slemr, F. (2010). Global atmospheric
 184 model for mercury including oxidation by bromine atoms. *Atmospheric Chemistry and Physics*, 10(24),
 185 12037–12057. <https://doi.org/10.5194/acp-10-12037-2010>
- 186 Lamborg, C. H., Von Damm, K. L., Fitzgerald, W. F., Hammerschmidt, C. R., & Zierenberg, R. (2006). Mercury
 187 and monomethylmercury in fluids from Sea Cliff submarine hydrothermal field, Gorda Ridge. *Geophysical*
 188 *Research Letters*, 33(17), L17606. <https://doi.org/10.1029/2006GL026321>
- 189 Lamborg, C. H., Hammerschmidt, C. R., Bowman, K. L., Swarr, G. J., Munson, K. M., Ohnemus, D. C., et al.
 190 (2014). A global ocean inventory of anthropogenic mercury based on water column measurements. *Nature*,
 191 512(7512), 65–68. <https://doi.org/10.1038/nature13563>
- 192 Lamborg, C. H., Hammerschmidt, C. R., & Bowman, K. L. (2016). An examination of the role of particles in
 193 oceanic mercury cycling. *Philosophical Transactions of the Royal Society A: Mathematical, Physical and*
 194 *Engineering Sciences*, 374(2081). <https://doi.org/10.1098/rsta.2015.0297>
- 195 Li, C., Sonke, J. E., Le Roux, G., Piotrowska, N., Van der Putten, N., Roberts, S. J., et al. (2020). Unequal
 196 Anthropogenic Enrichment of Mercury in Earth's Northern and Southern Hemispheres. *ACS Earth and*
 197 *Space Chemistry*, 4(11), 2073–2081. <https://doi.org/10.1021/acsearthspacechem.0c00220>
- 198 Obrist, D. (2012). Mercury Distribution across 14 U.S. Forests. Part II: Patterns of Methyl Mercury Concentrations
 199 and Areal Mass of Total and Methyl Mercury. *Environmental Science & Technology*, 46(11), 5921–5930.
 200 <https://doi.org/10.1021/es2045579>
- 201 Obrist, D., Pokharel, A. K., & Moore, C. (2014). Vertical Profile Measurements of Soil Air Suggest Immobilization
 202 of Gaseous Elemental Mercury in Mineral Soil. *Environmental Science & Technology*, 48(4), 2242–2252.
 203 <https://doi.org/10.1021/es4048297>
- 204 Olson, C. I., Geyman, B. M., Thackray, C. P., Krabbenhoft, D. P., Tate, M. T., Sunderland, E. M., & Driscoll, C. T.
 205 (2022). Mercury in soils of the conterminous United States: patterns and pools. *Environmental Research*
 206 *Letters*, 17(7), 074030. <https://doi.org/10.1088/1748-9326/ac79c2>
- 207 Shah, V., Jacob, D. J., Thackray, C. P., Wang, X., Sunderland, E. M., Dibble, T. S., et al. (2021). Improved
 208 Mechanistic Model of the Atmospheric Redox Chemistry of Mercury. *Environmental Science &*
 209 *Technology*, acs.est.1c03160. <https://doi.org/10.1021/acs.est.1c03160>
- 210 Smith-Downey, N. V., Sunderland, E. M., & Jacob, D. J. (2010). Anthropogenic impacts on global storage and
 211 emissions of mercury from terrestrial soils: Insights from a new global model. *Journal of Geophysical*
 212 *Research*, 115(G3), G03008. <https://doi.org/10.1029/2009JG001124>
- 213 Soerensen, A. L., Sunderland, E. M., Holmes, C. D., Jacob, D. J., Yantosca, R. M., Skov, H., et al. (2010). An
 214 Improved Global Model for Air-Sea Exchange of Mercury: High Concentrations over the North Atlantic.
 215 *Environmental Science & Technology*, 44(22), 8574–8580. <https://doi.org/10.1021/es102032g>

- 216 Sonke, J. E., Angot, H., Zhang, Y., Poulain, A., Björn, E., & Schartup, A. (2023). Global change effects on
217 biogeochemical mercury cycling. *Ambio*, 52(5), 853–876. <https://doi.org/10.1007/s13280-023-01855-y>
- 218 Streets, D. G., Horowitz, H. M., Jacob, D. J., Lu, Z., Levin, L., ter Schure, A. F. H., & Sunderland, E. M. (2017).
219 Total Mercury Released to the Environment by Human Activities. *Environmental Science & Technology*,
220 51(11), 5969–5977. <https://doi.org/10.1021/acs.est.7b00451>
- 221 Streets, D. G., Horowitz, H. M., Lu, Z., Levin, L., Thackray, C. P., & Sunderland, E. M. (2019). Five hundred years
222 of anthropogenic mercury: spatial and temporal release profiles*. *Environmental Research Letters*, 14(8),
223 084004. <https://doi.org/10.1088/1748-9326/ab281f>
- 224 Sunderland, E. M., & Mason, R. P. (2007). Human impacts on open ocean mercury concentrations. *Global*
225 *Biogeochemical Cycles*, 21(4). <https://doi.org/10.1029/2006GB002876>
- 226 Zhang, Y., Jacob, D. J., Dutkiewicz, S., Amos, H. M., Long, M. S., & Sunderland, E. M. (2015). Biogeochemical
227 drivers of the fate of riverine mercury discharged to the global and Arctic oceans. *Global Biogeochemical*
228 *Cycles*, 29(6), 854–864. <https://doi.org/10.1002/2015GB005124>
- 229